BELLE2-PUB-DRAFT-2023-010
Authors: Svenja Granderath, Jochen Dingfelder,
Peter Lewis, Florian Bernlochner

Intended journal: PRD
Draft version 8
May 2, 2024

Determination of $|V_{ub}|$ from simultaneous measurements of untagged $B^0 \to \pi^-\ell^+\nu_\ell$ and $B^+ \to \rho^0\ell^+\nu_\ell$ decays

We present a measurement of $|V_{ub}|$ from a simultaneous study of the charmless semileptonic decays $B^0 \to \pi^-\ell^+\nu_\ell$ and $B^+ \to \rho^0\ell^+\nu_\ell$, where $\ell = e, \mu$. This measurement uses a data sample of 387 million pairs of $B\overline{B}$ mesons recorded by the Belle II detector at the SuperKEKB electron-positron collider between 2019 and 2022. The two decays are reconstructed without identifying the partner B mesons. We simultaneously measure the differential branching fractions of $B^0 \to \pi^-\ell^+\nu_\ell$ and $B^+ \to \rho^0\ell^+\nu_\ell$ decays as functions of q^2 (momentum transfer squared). From these, we obtain total branching fractions $\mathcal{B}(B^0 \to \pi^-\ell^+\nu_\ell) = (1.516 \pm 0.042(\text{stat}) \pm 0.059(\text{syst})) \times 10^{-4}$ and $\mathcal{B}(B^+ \to \rho^0\ell^+\nu_\ell) = (1.625 \pm 0.079(\text{stat}) \pm 0.180(\text{syst})) \times 10^{-4}$. By fitting the measured $B^0 \to \pi^-\ell^+\nu_\ell$ partial branching fractions as functions of q^2, together with constraints on the non-perturbative hadronic contribution from lattice QCD calculations, we obtain $|V_{ub}| = (3.93 \pm 0.09 \pm 0.13 \pm 0.19) \times 10^{-3}$. Here, the first uncertainty is statistical, the second is systematic, and the third is theoretical.

PACS numbers:

I. INTRODUCTION

The Cabibbo-Kobayashi-Maskawa (CKM) [1, 2] matrix elements are related to four fundamental parameters of the Standard Model (SM) of particle physics. The magnitude of the matrix element V_{ub} can be determined by measuring the rate of $B \to X_u\ell\nu_\ell$ decays, which is proportional to $|V_{ub}|^2$, where X_u is a charmless hadronic final state and ℓ is a light charged lepton. Two methods can be used to measure $|V_{ub}|$. In the inclusive method, no specific X_u final state is reconstructed, and the sum of all possible final states is analyzed. The theoretical description involves calculation of the total semileptonic rate. In the exclusive method, a specific final state is reconstructed and the theoretical description takes the form of parametrizations of the low-energy strong interactions (form factors). These two methods have complementary uncertainties introduced by their theoretical descriptions. Determinations of $|V_{ub}|$ from experimental data obtained by the two methods currently differ by approximately 2.5 standard deviations [3].

The most experimentally and theoretically reliable exclusive measurements of $|V_{ub}|$ come from $B \to \pi\ell\nu_\ell$ decays. The current world average of $|V_{ub}|$ from this mode, taking all of the experimental and theoretical information into consideration, is $(3.67 \pm 0.09 \pm 0.12) \times 10^{-3}$ [3], where the first uncertainty is experimental and the second is theoretical. A simultaneous measurement of $B^0 \to \pi^-\ell^+\nu_\ell$ with $B \to \rho\ell\nu_\ell$ decays allows for an additional measurement of $|V_{ub}|$ while accounting for decays of one type that are reconstructed as the other. Therefore, we simultaneously reconstruct $B^0 \to \pi^-\ell^+\nu_\ell$ and $B^+ \to \rho^0\ell^+\nu_\ell$ (with charge conjugation implied throughout), focusing on decays with entirely charged final states in order to avoid backgrounds associated with neutral particles. We measure the differential branching fractions of these decays as a function of q^2, the squared momentum transferred from the B meson to the hadron. We use data from the Belle II detector located at the SuperKEKB electron-positron collider at KEK, in Japan. The B-meson decays are reconstructed in $e^+e^- \to \Upsilon(4S) \to B\overline{B}$ events. The reconstruction method employed here is called untagged, as the signal lepton and hadron candidates are selected without prior reconstruction (tagging) of the partner B meson. This leads to a high signal efficiency, but also a low purity due to the large combinatorial background from the partner B meson and increased backgrounds from e^+e^- collisions that produce light quark pair (continuum) events.

We reconstruct $B^0 \to \pi^-\ell^+\nu_\ell$ and $B^+ \to \rho^0\ell^+\nu_\ell$ events and make signal selections that reduce backgrounds. For both modes we build three-dimensional histograms of two kinematic variables plus reconstructed q^2. From simulation, we define $B^0 \to \pi^-\ell^+\nu_\ell$ and $B^+ \to \rho^0\ell^+\nu_\ell$ signal categories based on 13 and 10 disjoint intervals (bins) of simulated q^2, respectively. Signal templates defined in this way, which we refer to as true q^2 binning, can overlap in reconstructed q^2 due to resolution effects. We extract signal yields in all 23 signal categories with a simultaneous extended maximum-likelihood fit to both histograms. From these, we obtain differential branching fractions as functions of true q^2. We then combine constraints from theoretical form-factor predictions from unquenched lattice QCD (LQCD) [4] and light-cone sum rule (LCSR) [5, 6] calculations with the measured differential branching fractions to determine $|V_{ub}|$.

II. THEORETICAL FRAMEWORK

Accessing $|V_{ub}|$ through semileptonic $B \to X_u\ell\nu_\ell$ decays has the advantage over hadronic decays that the

leptonic and hadronic parts of the decay matrix element factorize at leading electroweak order. However, the description of the hadronic contribution to the matrix element has many uncertainties, since higher-order perturbative corrections and hadronization processes need to be included. Form factors parametrize these QCD processes in the full phase-space and are constrained in specific phase-space regions by theoretical predictions based on, for example, LQCD and LCSR calculations [7]. These predictions rely on the $V-A$ structure of the process and are usually formulated as functions of q^2. For the semileptonic decay $B \to X\ell\nu_\ell$,

$$q^2 = (p_B - p_X)^2, \tag{1}$$

where p_B and p_X are the four-momenta of the B meson and the hadron, respectively. Here we use natural units with $c = 1$ throughout. LQCD predictions rely on first principles to predict the form factors for $B \to \pi\ell\nu_\ell$, and are only available in the high-q^2 region. LCSR predictions, on the other hand, are only applicable in the low-q^2 region, but are available for $B \to \pi\ell\nu_\ell$ and $B \to \rho\ell\nu_\ell$ decays.

In the theoretical description of the kinematic processes as a function of q^2, it is necessary to distinguish between decays into pseudoscalar and vector mesons, such as $B \to \pi\ell\nu_\ell$ and $B \to \rho\ell\nu_\ell$, respectively. The hadronic matrix element of the decay $B \to \pi\ell\nu_\ell$ can be written in terms of two form factors $f_+(q^2)$ and $f_0(q^2)$, where $f_0(q^2)$ is negligible in case $\ell = e, \mu$. The differential decay rate can then be expressed as a function of $f_+(q^2)$ and $|V_{ub}|$ [7]:

$$\frac{\mathrm{d}\Gamma(B \to \pi\ell\nu_\ell)}{\mathrm{d}q^2 \mathrm{d}\cos\theta_{W\ell}} = |V_{ub}|^2 \frac{G_F^2 |\vec{p}_\pi|^3}{32\pi^3} \sin^2\theta_{W\ell} |f_+(q^2)|^2, \tag{2}$$

where G_F is the Fermi constant, $\vec{p}_\pi$ is the momentum of the pion in the B-meson rest frame, and $\theta_{W\ell}$ is the angle between the W boson momentum in the B rest frame and the lepton momentum in the W rest frame.

The hadronic matrix element of $B \to \rho\ell\nu_\ell$ is described by four form factors, which can be reduced to three, $A_1(q^2)$, $A_2(q^2)$, and $V(q^2)$, for decays to light leptons ($\ell = e, \mu$). The form factors can be rewritten in terms of the helicity amplitudes, $H_+(q^2)$, $H_-(q^2)$, and $H_0(q^2)$, of the ρ meson. The differential decay rate as a function of $H_\pm$, $H_0(q^2)$, and $|V_{ub}|$ then becomes [7]:

$$\begin{aligned}\frac{\mathrm{d}\Gamma(B \to \rho\ell\nu_\ell)}{\mathrm{d}q^2 \mathrm{d}\cos\theta_{W\ell}} &= |V_{ub}|^2 \frac{G_F^2 |\vec{p}_\rho| q^2}{128\pi^3 m_B^2} \\ &\times \left[\sin^2\theta_{W\ell} |H_0(q^2)|^2 + (1 - \cos\theta_{W\ell})^2 \frac{|H_+(q^2)|^2}{2} \right. \\ &\left. + (1 + \cos\theta_{W\ell})^2 \frac{|H_-(q^2)|^2}{2} \right], \end{aligned} \tag{3}$$

where m_B is the mass of the B meson, and $\vec{p}_\rho$ is the momentum of the ρ meson in the B rest frame.

Due to the relationship between the differential decay rate of $B \to \pi\ell\nu_\ell$ (or $B \to \rho\ell\nu_\ell$), $|V_{ub}|$, and the respective form factors, $|V_{ub}|$ can be extracted from measurements of the differential decay rates of $B \to \pi\ell\nu_\ell$ (or $B \to \rho\ell\nu_\ell$) if the q^2 shape and normalizations of the form factors are known. The normalizations are provided by theoretical QCD calculations of the form factors. Since these calculations are not available across the entire q^2 range, the q^2 dependence of the form factors is interpolated between the high and low-q^2 regions using analyticity and unitarity arguments. One technique employs dispersion relations to expand in powers of the variable $z(q^2, q_0^2)$ defined as

$$z(q^2, q_0^2) = \frac{\sqrt{m_+^2 - q^2} - \sqrt{m_+^2 - q_0^2}}{\sqrt{m_+^2 - q^2} + \sqrt{m_+^2 - q_0^2}}, \tag{4}$$

where $m_+ = m_B + m_X$ is the sum of the masses of the B meson and the hadron. According to Ref. [8] the optimal choice of the parameter q_0^2 is given by $q_0^2 = m_+(\sqrt{m_B} - \sqrt{m_X})^2$.

Two expansion parametrizations are considered in this work. The first parametrization is the Bourrely-Caprini-Lellouch (BCL) parametrization [8], which expands the form factor $f_+(q^2)$ using form-factor coefficients b_k^+ up to expansion order K as:

$$f_+(q^2) = P(q^2) \sum_{k=0}^{K-1} b_k^+ \left[z^k - (-1)^{k-K} \frac{k}{K} z^K \right]. \tag{5}$$

Here $P(q^2) = (1 - q^2/m_R^2)^{-1}$ is called the inverse Blaschke factor, where the mass of the resonance m_R depends on the allowed angular momentum and parity. The expansion of the form factor $f_0(q^2)$ using form-factor coefficients b_k^0 takes the form:

$$f_0(q^2) = f_+(0) \left[1 + \sum_{k=0}^{K-1} b_k^0 z^k \right]. \tag{6}$$

The Bharucha-Straub-Zwicky (BSZ) parametrization [6] instead is a series expansion around $q^2 = 0$, using form-factor coefficients b_k^i, so that the form factors $f_i(q^2) \in \{A_1(q^2), A_2(q^2), V(q^2)\}$ take the form

$$f_i(q^2) = P(q^2) \sum_{k=0}^{K-1} b_k^i \Big(z(q^2) - z(0) \Big)^k. \tag{7}$$

By fitting the form-factor parametrizations given in Equations 5, 6 and 7 to measured partial branching-fraction spectra, the form-factor coefficients b_k^i can be extracted. In addition, by adding theoretical input from LCSR or LQCD calculations, we can determine $|V_{ub}|$.

III. DETECTOR, DATA SET, AND SIMULATION

A. Detector

The Belle II experiment [9] is located at SuperKEKB, which collides electrons and positrons at and near the

$\Upsilon(4S)$ resonance [10]. The Belle II detector [9] has a cylindrical geometry and includes a two-layer silicon-pixel detector (PXD) surrounded by a four-layer double-sided silicon-strip detector (SVD) [11] and a 56-layer central drift chamber (CDC). These detectors reconstruct trajectories (tracks) of charged particles. Only one sixth of the second layer of the PXD was installed for the data analyzed here. The symmetry axis of these detectors, defined as the z axis, is almost coincident with the direction of the electron beam. Surrounding the CDC, which also provides $\mathrm{d}E/\mathrm{d}x$ energy-loss measurements and has a polar angle acceptance of 17–150°, is a time-of-propagation counter (TOP) [12] in the central region and an aerogel-based ring-imaging Cherenkov counter (ARICH) in the forward region. These detectors provide charged-particle identification. Surrounding the TOP and ARICH is an electromagnetic calorimeter (ECL) based on CsI(Tl) crystals that primarily provides energy and timing measurements for photons and electrons. Outside of the ECL is a superconducting solenoid magnet. Its flux return is instrumented with resistive-plate chambers and plastic scintillator modules to detect muons, K_L^0 mesons, and neutrons. The solenoid magnet provides a 1.5 T magnetic field that is parallel to the z axis.

Using $\mathrm{d}E/\mathrm{d}x$ energy-loss data from the CDC and information from the two particle-identification detectors, the ARICH and TOP, as well as data from the ECL, the SVD, and the K_L^0 and muon detector (KLM), charged particles of different masses are identified via particle-identification (PID) likelihood ratios. Each of these is a ratio of the likelihood $\mathcal{L}$ for one charged-particle hypothesis α to the sum of the likelihoods for all hypotheses: $\mathrm{PID}_\alpha = \mathcal{L}_\alpha/(\mathcal{L}_e + \mathcal{L}_\mu + \mathcal{L}_\pi + \mathcal{L}_K + \mathcal{L}_p + \mathcal{L}_d)$, where $\alpha \in \{e, \mu, \pi, K,$ proton $(p),$ deuteron $(d)\}$. The identification efficiencies and misidentification probabilities of the pion, kaon, electron, and muon likelihood ratios are determined separately for both charges in bins of momentum and polar angle using data samples of control modes, such as $J/\psi \to \ell^+\ell^-$ and $D^{*+} \to \overline{D}^0[\to K^-\pi^+]\pi^+$.

B. Experimental data

The primary data set used in this analysis consists of (387 ± 6) million $\Upsilon(4S) \to B\overline{B}$ events from (364 ± 2) fb^{-1} of electron-positron collisions collected at a center-of-mass (c.m.) energy of $\sqrt{s} = 10.58$ GeV, corresponding to the $\Upsilon(4S)$ resonance. We use an additional sample corresponding to (42.6 ± 0.3) fb^{-1} of off-resonance collision data, collected at a c.m. energy 60 MeV below the $\Upsilon(4S)$ resonance, to describe background from continuum processes. These include $q\overline{q}$ production $e^+e^- \to u\bar{u}$, $d\bar{d}$, $s\bar{s}$, and $c\bar{c}$, QED processes such as $e^+e^- \to \tau^+\tau^-$, and two-photon processes such as $e^+e^- \to e^+e^-\ell^+\ell^-$ and $e^+e^- \to e^+e^-\pi^+\pi^-$.

C. Simulation

We use simulated data sets referred to as Monte Carlo (MC) samples to identify efficient background-discriminating variables and to form fit templates for signal extraction. The MC samples for $B\overline{B}$ background events correspond to an integrated luminosity of 3 ab^{-1} and contain semileptonic and hadronic B decays, generated using the `EvtGen` [13] software package.

We use generated signal MC samples containing 10 million events of $B^0 \to \pi^-\ell^+\nu_\ell$ and $B^+ \to \rho^0\ell^+\nu_\ell$ decays to obtain reconstruction efficiencies and study the key kinematic distributions. In order to describe the remaining $B \to X_u\ell\nu_\ell$ decays, we simulate four samples, each containing 50 million events, of resonant and nonresonant $B^0 \to X_u^-\ell^+\nu_\ell$, and $B^+ \to X_u^0\ell^+\nu_\ell$. The resonant sample contains $B \to X_u\ell\nu_\ell$ decays, where $X_u \in \{\pi, \rho, \omega, \eta, \eta'\}$. We simulate the hadronization of the X_u state to multiple hadrons in nonresonant $B \to X_u\ell\nu_\ell$ events with `PYTHIA` [14]. The second B meson decays in the same way as the generic $B\overline{B}$ background described above.

We further generate 1 ab^{-1} of $q\overline{q}$ and $\tau\tau$ continuum-event samples with `KKMC` [15], and simulate $q\overline{q}$ fragmentation with `PYTHIA` [14] and τ decays with `TAUOLA` [16]. Additionally, we simulate 2 ab^{-1} of two-photon production with `AAFH` [17]. Final-state radiation of photons from stable charged particles is simulated with `PHOTOS` [18] and we overlay simulated beam-induced backgrounds to all generated events [19]. The propagation of particles through the detector and the resulting interactions are simulated using `Geant4` [20]. We reconstruct and analyze simulated and experimental data with the Belle II analysis software framework, `basf2` [21, 22].

In the simulation of $B\overline{B}$ backgrounds, we use world-average $B \to X\ell\nu_\ell$ branching fractions [23] in combination with an isospin-symmetry assumption, following the procedure in Ref. [24] for $B \to X_c\ell\nu_\ell$ decays. We assume that the remaining difference between the sum of the exclusive $B \to X_c\ell\nu_\ell$ decay branching fractions and the measured total branching fraction, accounting for approximately 4% of the $B \to X_c\ell\nu_\ell$ decays, is saturated by $B \to D^{(*)}\eta\ell\nu_\ell$ decays, which corresponds to the procedure in Ref. [25]. For the form factors of $B \to D\ell\nu_\ell$ and $B \to D^*\ell\nu_\ell$ decays, we use the Boyd-Grinstein-Lebed parametrization (BGL) [26] with central values from Ref. [27] and [28], respectively.

For $B \to X_u\ell\nu_\ell$ decays, the sum of the measured exclusive branching fractions is approximately 20% of the inclusively measured branching fraction. We model the remaining difference with nonresonant $B \to X_u\ell\nu_\ell$ decays. An important component of these nonresonant $B \to X_u\ell\nu_\ell$ decays are events in which the X_u system consists of a $\pi^+\pi^-$ pair. The partial-branching-fraction spectrum of $B^+ \to \pi^+\pi^-\ell^+\nu_\ell$ as a function of the dipion invariant mass $m_{\pi\pi}$ has been measured in Ref. [29]. We compare this experimental spectrum to the simulated spectrum of nonresonant $B^+ \to \pi^+\pi^-\ell^+\nu_\ell$ events. As-

suming that the nonresonant $B \to X_u \ell \nu_\ell$ events have no structure below the ρ^0 mass peak, we interpolate the measured spectrum to the ρ^0 mass peak window by fitting a straight line with floating slope and intercept to the spectrum surrounding the peak. We then assign event weights to the simulated $B^+ \to \pi^+\pi^-\ell^+\nu_\ell$ events in order to recover the measured partial branching fractions as a function of $m_{\pi\pi}$ in the simulation.

We describe the remaining nonresonant $B \to X_u \ell \nu_\ell$ decays with the De Fazio and Neubert (DFN) model [30], which combines a prediction of the triple-differential rate in X_u particle mass m_X, the B rest-frame lepton energy E_ℓ, and q^2, with a non-perturbative shape function using an exponential model. In the simulation we use central values for the two relevant parameters provided in Ref. [31]. The total $B \to X_u \ell \nu_\ell$ composition is described by implementing a hybrid model [32], following closely the method in Ref. [33]. This approach combines the exclusive and nonresonant decay rates in bins of m_X, E_ℓ, and q^2, in order to reproduce the inclusive rates.

We describe $B \to \pi \ell \nu_\ell$ decays using the BCL parametrization [8] with central values for the parameters b_k^+ and b_k^0 in Equations 5 and 6, respectively, from Ref [4], and $B \to \rho \ell \nu_\ell$ and $B \to \omega \ell \nu_\ell$ decays using the BSZ parametrization [6] with central values for b_k^i in Equation 7 from Ref. [34]. The lineshape of the ρ meson is modeled following the description in Ref. [35] neglecting interference between the ρ and the ω meson, which is included as a systematic uncertainty and described in Section VII. For the form-factor description of $B \to \eta^{(\prime)} \ell \nu_\ell$ decays we use a LCSR calculation [36].

IV. EVENT RECONSTRUCTION AND SELECTION

A. Signal reconstruction and selection

We begin signal reconstruction by identifying track candidates that pass certain quality criteria. The extrapolated trajectories must originate from a cylindrical region of length 3 cm along the z axis and radius 0.5 cm in the transverse plane, centered on the e^+e^- interaction point. Furthermore, charged particles must have a transverse momentum greater than 0.05 GeV and polar angles within the CDC acceptance. We discard events with fewer than five tracks satisfying the above criteria.

In the remaining events, we select signal-lepton candidates from among the selected tracks by requiring that their c.m. momentum p_ℓ^* is in the range $[1.0, 2.85]$ GeV and $[1.4, 2.85]$ GeV in the $B^0 \to \pi^-\ell^+\nu_\ell$ and $B^+ \to \rho^0\ell^+\nu_\ell$ modes, respectively. These selections significantly reduce the number of events in which the lepton originates from $B \to X_c \ell \nu_\ell$ decays, where X_c is a hadronic final state containing a charm quark. We choose a higher lepton momentum threshold for $B^+ \to \rho^0\ell^+\nu_\ell$ candidates, since, due to the different spin structure, the lepton momentum spectrum of $B^+ \to \rho^0\ell^+\nu_\ell$ peaks at a higher momentum than that of $B^0 \to \pi^-\ell^+\nu_\ell$. In order to reduce sensitivity to detector response modeling in the extreme forward and backward directions of the lepton polar angle θ_ℓ, we exclude events with $\cos\theta_\ell < -0.55$ and $\cos\theta_\ell > 0.85$.

We require that electron and muon candidates have PID likelihood ratios greater than 0.9. The electron likelihood ratio combines information from the CDC, ECL, ARICH and the KLM, while the muon likelihood ratio also includes information from the TOP. The average electron (muon) efficiency is 92 (93)%. The hadron misidentification rates are 0.2% for the electron and 3.2% for the muon selection, respectively. The four-momenta of the electron candidates are corrected for bremsstrahlung by adding the four-momenta of photons with a cluster energy below 1.0 GeV for $B^0 \to \pi^-\ell^+\nu_\ell$ and 0.5 GeV for $B^+ \to \rho^0\ell^+\nu_\ell$ found within a cone of 0.05 rad around the electron-momentum vector.

In the $B^0 \to \pi^-\ell^+\nu_\ell$ mode we select pion candidates from the remaining tracks and require that they have a charge opposite to that of the lepton candidate. In the $B^+ \to \rho^0\ell^+\nu_\ell$ mode we require that the two selected pion candidates that compose the ρ candidate have opposite charges and combine with a mass $m_{\pi\pi}$ in the range $[0.554, 0.996]$ GeV. This selection reduces combinatorial background, but is loose enough to reduce sensitivity to modeling of the ρ mass distribution. We reduce sensitivity to the modeling of the detector response in the extreme backward region of pion polar angle θ_π by selecting pions with $\cos\theta_\pi > -0.65$. All pion candidates are required to have a PID likelihood ratio greater than 0.1. The pion likelihood, in addition to data from the CDC, ECL, ARICH and the KLM, includes information from the SVD and the TOP. To improve the particle-identification performance, we require that the pion candidates have at least 20 measurement points in the CDC. The resulting average pion efficiency is 86% with kaon and lepton misidentification rates of 7% and 0.4%, respectively.

The following selections are designed to reduce backgrounds and enhance signal purity in the selected sample. Next, we remove candidates with kinematic properties inconsistent with the signal B decay. Under the assumption that only a single massless particle is not included in the event reconstruction, the angle between the B and the combination of the signal lepton and hadron candidates, denoted Y, is determined,

$$\cos\theta_{\rm BY} = \frac{2E_B^* E_Y^* - m_B^2 - m_Y^2}{2|\vec{p}_B^*||\vec{p}_Y^*|}, \qquad (8)$$

where E_Y^*, $|\vec{p}_Y^*|$, and m_Y are the energy, magnitude of the three-momentum, and invariant mass of the Y in the c.m. frame, respectively. The energy E_B^* and the magnitude of the three-momentum $|\vec{p}_B^*|$ of the B are calculated from the beam properties, and m_B is the mass of the B [23]. For correctly reconstructed signal decays and assuming perfect resolution, we expect $\cos\theta_{\rm BY}$ to lie between -1 and 1. However, to retain enough background events to

train the classifiers discussed in Section V B, we choose a less restrictive requirement, $|\cos\theta_{\rm BY}| < 1.6$. Additionally, we perform vertex fits [37] to the hadron and lepton candidates and require that they converge.

B. Missing momentum reconstruction

We estimate the momentum of the signal neutrino by attributing the sum of the remaining tracks and electromagnetic energy-depositions (clusters) in the event, called the rest of event (ROE), to the partner B. From energy and momentum conservation, we construct a missing four-momentum in the c.m. frame,

$$(E^*_{\rm miss}, \vec{p}^*_{\rm miss}) = (E^*_{\Upsilon(4S)}, \vec{p}^*_{\Upsilon(4S)}) - \left(\sum_i E^*_i, \sum_i \vec{p}^*_i\right), \quad (9)$$

where E^*_i and $\vec{p}^*_i$ correspond to the c.m. energy and momentum of the ith track or cluster in the event, respectively. We determine E^*_i using the momentum derived from the reconstructed track and selecting the mass hypothesis m_α that corresponds to the highest probability of identification PID_α. We attribute the missing four-momentum to the signal neutrino, with momentum $\vec{p}^*_\nu = \vec{p}^*_{\rm miss}$, and energy, $E^*_\nu = |\vec{p}^*_\nu| = |\vec{p}^*_{\rm miss}|$. Taking the magnitude of $\vec{p}^*_{\rm miss}$, instead of $E^*_{\rm miss}$, to approximate the neutrino energy, leads to an improvement in resolution of 15%. While reconstruction losses add up linearly in the calculation of $E^*_{\rm miss}$, this is not the case for the vector sum calculation of $\vec{p}^*_{\rm miss}$.

Since all reconstructed tracks and clusters contribute to the resolution of the neutrino momentum estimation, obtaining an ROE as pure and complete as possible is critical. To reduce the impact of clusters from beam-induced backgrounds, acceptance losses, or other effects, we impose quality criteria for objects to be included in the ROE. We only consider clusters that are within the CDC acceptance with energies in forward, barrel, and backward directions greater than 0.060, 0.050, and 0.075 GeV, respectively. We require that the clusters contain more than one calorimeter crystal and are detected within 200 ns of the collision time, which is approximately five times the mean timing resolution of the calorimeter. In addition to removing background particles from the ROE, we must account for particles that may escape undetected. To reduce the impact of these events, we require that the polar angle of the missing momentum in the laboratory frame $\theta_{\rm miss}$ is within the CDC acceptance.

C. Signal extraction variables

We reconstruct q^2 from Equation 1, and thus need to estimate the B momentum vector. One existing method, called the Diamond Frame [38], takes the weighted average of four possible $\vec{p}^*_B$ vectors uniformly distributed in azimuthal angle on the cone defined by $\cos\theta_{\rm BY}$, weighting by the $\sin^2\theta_B$ distribution, which expresses the prior probability of the B flight direction in $\Upsilon(4S)$ decays with respect to the electron-positron beam axis. A second method, called the ROE method [39], assumes the signal B momentum vector to be the vector on the $\cos\theta_{\rm BY}$ cone that is closest to antiparallel to the ROE momentum vector $\vec{p}^*_{\rm ROE}$. There is a third method [40] that combines these two by multiplying the Diamond Frame weights by $\frac{1}{2}(1-\hat{p}^*_B\cdot\hat{p}^*_{\rm ROE})$ and averaging over ten vectors uniformly distributed on the cone, where $\hat{p}^*_B$ and $\hat{p}^*_{\rm ROE}$ denote the unit vectors of $\vec{p}^*_B$ and $\vec{p}^*_{\rm ROE}$, respectively. We adopt this combined method because, in simulation, it assigns reconstructed signal candidates to the correct q^2 bin more often than other methods do, leading to a reduction in the bin migrations of up to 2%. The resolutions in q^2 decrease with increasing q^2 and range from 0.09–0.60 GeV^2 in the $B^0 \to \pi^-\ell^+\nu_\ell$ mode, and from 0.16–0.84 GeV^2 in the $B^+ \to \rho^0\ell^+\nu_\ell$ mode.

We divide B candidates into 13 reconstructed q^2 bins in the $B^0 \to \pi^-\ell^+\nu_\ell$ mode and into 10 bins in the $B^+ \to \rho^0\ell^+\nu_\ell$ mode. The lowest bin boundary is at 0, and the first 12 (9) bins have uniform bin widths of 2 GeV^2 in the $B^0 \to \pi^-\ell^+\nu_\ell$ ($B^+ \to \rho^0\ell^+\nu_\ell$) mode. The last bins extend to the kinematic limits of 26.4 GeV^2 in the $B^0 \to \pi^-\ell^+\nu_\ell$ mode and 20.3 GeV^2 in the $B^+ \to \rho^0\ell^+\nu_\ell$ mode. The following are the labels and bin edges for the q^2 bins: $q1 : q^2 \in [0,2]$, $q2 : [2,4]$, $q3 : [4,6]$, $q4 : [6,8]$, $q5 : [8,10]$, $q6 : [10,12]$, $q7 : [12,14]$, $q8 : [14,16]$, $q9 : [16,18]$, $q10 : [18,20(20.3)]$, $q11 : [20,22]$, $q12 : [22,24]$, $q13 : [24,26.4]$ GeV^2.

Two further variables that test the kinematic consistency of a candidate with a signal B decay using ROE information are the beam-constrained mass, defined as

$$M_{\rm bc} = \sqrt{E^{*2}_{\rm beam} - |\vec{p}^*_B|^2} = \sqrt{\left(\frac{\sqrt{s}}{2}\right)^2 - |\vec{p}^*_B|^2} \quad (10)$$

and the energy difference, defined as

$$\Delta E = E^*_B - E^*_{\rm beam} = E^*_B - \frac{\sqrt{s}}{2}, \quad (11)$$

where $E^*_{\rm beam}$, E^*_B and $\vec{p}^*_B$ are the single-beam energy, the reconstructed B energy, and the reconstructed B momentum, all determined in the $\Upsilon(4S)$ rest frame, respectively. The reconstructed B energy (momentum) is given by the sum of the reconstructed energies (momenta) of the signal lepton and hadron candidates and the inferred neutrino energy (momentum) described above. We define a fit region in ΔE and $M_{\rm bc}$, corresponding to $-0.95 < \Delta E < 1.25$ GeV and $5.095 < M_{\rm bc} < 5.295$ GeV. This region is enriched in signal, but at the same time includes background-enhanced regions to allow sufficient discrimination between signal and background.

V. BACKGROUND SUPPRESSION

A. Signal and background categories

As explained in Section III C, the simulated samples can be separated into two main categories: $B\overline{B}$ events and continuum events. For the $B\overline{B}$ events we define a subcategory that combines true signal and combinatorial signal events. In combinatorial signal either the signal hadron or lepton candidate is incorrectly chosen. In addition, we define an isospin-conjugate signal category, where the lepton originates from the isospin conjugate of the signal decay. The branching fraction of the isospin-conjugate signal events scales with the branching fraction of true signal events under the assumption of isospin symmetry:

$$\mathcal{B}(B^0 \to \pi^- \ell^+ \nu_\ell) = 2\tau_0/\tau_+ \times \mathcal{B}(B^+ \to \pi^0 \ell^+ \nu_\ell),$$
$$\mathcal{B}(B^0 \to \rho^- \ell^+ \nu_\ell) = 2\tau_0/\tau_+ \times \mathcal{B}(B^+ \to \rho^0 \ell^+ \nu_\ell),$$

where τ_+/τ_0 is the B lifetime ratio.

A fourth signal category, called cross-feed signal, includes events where the lepton originates from the reconstructed signal decay mode, but it was reconstructed in the other signal mode, i.e. $B \to \rho\ell\nu_\ell$ events reconstructed in the $B \to \pi\ell\nu_\ell$ sample, and vice versa. Since the number of true, combinatorial, and ispospin-conjugate signal events scales with the same branching fraction as the cross-feed signal events from the other reconstructed mode, we combine the four signal categories into a total signal category.

We further split the remaining $B\overline{B}$ events into the two largest semileptonic backgrounds, $B \to X_c\ell\nu_\ell$ and $B \to X_u\ell\nu_\ell$. The remaining $B\overline{B}$ events are combined into the *other* $B\overline{B}$ category, which is mainly composed of candidates with misidentified leptons, or with leptons from secondary decays.

B. Background suppression using boosted decision trees

In order to further reduce the $B\overline{B}$ and continuum backgrounds, we train boosted decision trees (BDTs) to separate signal from these two background categories using FastBDT [41]. Since the background composition is different between the $B^0 \to \pi^-\ell^+\nu_\ell$ and $B^+ \to \rho^0\ell^+\nu_\ell$ modes, and between the q^2 bins, we train the classifier and optimize the selection separately for each q^2 bin and mode. Additionally, to increase the sensitivity in the highest q^2 bin in the $B^+ \to \rho^0\ell^+\nu_\ell$ mode, we split the last bin into two bins during training and optimization of the selection. Due to training separate classifiers for the suppression of continuum and $B\overline{B}$ backgrounds, we train a total of $2 \times (13+11) = 48$ BDTs. In each training we use equal amounts of true signal and background simulation events, corresponding to 400 fb^{-1} of continuum simulated data, and 1 ab^{-1} of $B\overline{B}$ simulated data.

We use event-shape, kinematic and topological variables as BDT input variables. The event-shape input variables includes four normalized Fox-Wolfram moments [42] and variables based on the thrust axis, which is the axis that maximizes the sum of the projected momenta of a collection of particles in the event [43]. Distinct thrust axes can be defined for the signal B and the ROE. Their magnitudes, the angle between the two axes $\cos\theta_T$, and the angle between the signal B thrust axis and the beam direction serve as input variables. Three cones with opening angles of 10°, 20°, and 30° centered around the signal B thrust axis are defined, and the momentum flow into each of the three cones is added as an input variable [44].

The kinematic and topological variables include the χ^2 probability of the vertex fit to the pion and lepton candidates, the cosine of the angle between the signal B momentum vector, and the vector connecting its fitted vertex to the interaction point in the plane parallel and perpendicular to the beam axis. Other input variables are $\cos\theta_{\rm BY}$, $\theta_{\rm miss}$, the number of tracks, the momentum of the ROE, and the polar angle of the lepton candidate. The remaining variables are the angle between the direction of the lepton in the W frame and the W in the B frame, and for the $B^+ \to \rho^0\ell^+\nu_\ell$ mode, the angle between the ρ in the B frame and the pion in the ρ rest frame.

We train each of the 48 BDTs using the twelve input variables that provide the highest discriminating power in the corresponding q^2 bin, and ensure that none of the selected input variables are strongly correlated with ΔE or $M_{\rm bc}$. The input variable with the most discriminating power for the suppression of continuum events is $\cos\theta_T$, while $\cos\theta_{\rm BY}$ and the χ^2 vertex fit probability are the input variables with the most discriminating power for the suppression of $B\overline{B}$ events. We identify the optimal selection criterion on the combination of the continuum and $B\overline{B}$ output classifiers within each q^2 bin by maximizing the ratio between the number of signal events and the square root of the sum of the number of signal and background events, as predicted by simulation. In the $B^0 \to \pi^-\ell^+\nu_\ell$ ($B^+ \to \rho^0\ell^+\nu_\ell$) mode these selections retain 55%(48%) of the signal, 4%(1%) of the $B\overline{B}$ background, and 1%(0.6%) of the continuum background.

C. Continuum reweighting

Because of the small size of the off-resonance data, especially after suppressing continuum events, using it directly to construct fit templates results in large statistical fluctuations in the individual bins. Instead, we weight the simulated continuum candidates using off-resonance data in order to use the resulting template during signal extraction. To produce the weights we initially compare the q^2 shapes of simulated continuum data and off-resonance data, where we account for the difference in cross section between the on- and the off-resonance data

sets. We observe similar normalization differences in the $B^0 \to \pi^-\ell^+\nu_\ell$ and $B^+ \to \rho^0\ell^+\nu_\ell$ modes, corresponding to a ratio between the number of events in off-resonance to simulated data of 1.2. After correcting the simulated continuum data for the total normalization, differences in the q^2 and ΔE spectra remain. These residual differences are removed by correcting the simulated two-dimensional q^2 and ΔE spectra using bin-by-bin event weights defined as the ratio between the number of off-resonance events and the number of simulated continuum events in each bin. This approach relies on the assumption that the difference between off-resonance data and the simulated continuum sample is independent of $M_{\rm bc}$. We validate this assumption and verify the reweighting procedure by obtaining reasonable p-values from χ^2 tests on the distributions of ΔE and $M_{\rm bc}$ in the reweighted simulated and off-resonance data. The systematic uncertainty assigned to the limited size of off-resonance data is explained in Section VII.

D. Selection summary

At this stage, an average of 1.08 (1.18) candidates remain for each selected event in the $B^0 \to \pi^-\ell^+\nu_\ell$ ($B^+ \to \rho^0\ell^+\nu_\ell$) mode. Some of the events are also reconstructed in both modes. In events with multiple candidates in both or either of the modes, we randomly select one and discard the rest. In this way we ensure that a single event cannot contribute multiple times to either or both of the $B^0 \to \pi^-\ell^+\nu_\ell$ and $B^+ \to \rho^0\ell^+\nu_\ell$ modes.

We divide the simulated signal events into categories based on their true q^2 values, using the same intervals as the reconstructed q^2 bins described in Section IV C. We define the signal efficiency as the fraction of signal events generated in a given true q^2 interval that survive all selections, regardless of whether they are reconstructed in the same q^2 interval. In simulation, these efficiencies range from 9% to 19% in the $B^0 \to \pi^-\ell^+\nu_\ell$ mode and from 3% to 9% in the $B^+ \to \rho^0\ell^+\nu_\ell$ mode. We call the ratio between the number of true and combinatorial signal events and the total number of signal events the signal strength. Depending on the true q^2 bin, the signal strength is between 69% and 99% in the $B^0 \to \pi^-\ell^+\nu_\ell$ mode and between 23% and 57% in the $B^+ \to \rho^0\ell^+\nu_\ell$ mode. The distributions of ΔE and $M_{\rm bc}$ integrated over the 13 (10) reconstructed q^2 bins for $B^0 \to \pi^-\ell^+\nu_\ell$ ($B^+ \to \rho^0\ell^+\nu_\ell$) decays after all selections are shown in Fig. 1.

VI. SIGNAL EXTRACTION

A. Fit method

We extract the $B^0 \to \pi^-\ell^+\nu_\ell$ and $B^+ \to \rho^0\ell^+\nu_\ell$ signal yields by performing a simultaneous extended maximum likelihood fit to the binned three-dimensional distributions of ΔE, $M_{\rm bc}$ and reconstructed q^2. We divide the ΔE and $M_{\rm bc}$ distributions into 5 and 4 bins, respectively. The corresponding bin widths vary, where smaller bins are used in the signal-rich regions. The binning is chosen so that a clear separation of signal and background is achieved, while ensuring a sufficient number of events populate each bin. This results in 20 bins per reconstructed q^2 bin, and therefore a total of $20 \times [13\ (B^0 \to \pi^-\ell^+\nu_\ell) + 10\ (B^+ \to \rho^0\ell^+\nu_\ell)] = 460$ bins.

The background in each signal mode is treated separately and split into four components according to the description in Section V A. The fit parameters include unconstrained scale factors $b_p^{(\pi/\rho)}$ for each mode $(\pi/\rho)\ell\nu$ and each background component p. The background templates are constructed from simulated $B\overline{B}$ data and the reweighted continuum data. We introduce Gaussian penalty factors to constrain the continuum yields to the scaled off-resonance yields.

In addition to the background templates, we also have one independent total signal template for each true q^2 bin i and each mode, resulting in 23 signal templates with unconstrained scale factors s_i^π and s_i^ρ. Because these templates are defined based on true q^2 categories, they naturally account for resolution effects that could cause events that are generated in one q^2 bin to be reconstructed in another. The composition of the total signal component was described in Section V A. In this way, the $B^0 \to \pi^-\ell^+\nu_\ell$ background in the $B^+ \to \rho^0\ell^+\nu_\ell$ mode is linked with the $B^0 \to \pi^-\ell^+\nu_\ell$ signal in the $B^0 \to \pi^-\ell^+\nu_\ell$ mode, and vice versa. The signal templates are constructed from simulated signal events. The contribution of true and combinatorial signal to the total signal templates, the signal strength, is inferred from simulation. A summary of the 31 templates and scale factors is given in Table I.

Table I: Summary of the templates and corresponding scale factors determined from the fit for the different background sources and signal samples. There is one signal scale factor for each true q^2 bin i and each signal decay, where $i \in [1, 13]$ for s_i^π and $i \in [1, 10]$ for s_i^ρ. All fit parameters are free, with $b^\pi_{\rm cont}$ and $b^\rho_{\rm cont}$ constrained by off-resonance data.

Component		Reconstructed mode $B^0 \to \pi^-\ell^+\nu_\ell$	Reconstructed mode $B^+ \to \rho^0\ell^+\nu_\ell$
Signal:	True signal	s_i^π	s_i^ρ
	Comb. signal	s_i^π	s_i^ρ
	Isospin-c. signal	s_i^π	s_i^ρ
	Cross-feed	s_i^ρ	s_i^π
Background:	$B \to X_u\ell\nu_\ell$	$b^\pi_{X_u\ell\nu}$	$b^\rho_{X_u\ell\nu}$
	$B \to X_c\ell\nu_\ell$	$b^\pi_{X_c\ell\nu}$	$b^\rho_{X_c\ell\nu}$
	Other $B\overline{B}$	$b^\pi_{B\overline{B}}$	$b^\rho_{B\overline{B}}$
	Continuum	$b^\pi_{\rm cont}$	$b^\rho_{\rm cont}$

The likelihood to be maximized is

$$\mathcal{L}(\vec{S}, \vec{B}) = \prod_l \text{Poisson}(N_l | \sum_j S_{lj} + \sum_k B_{lk}), \qquad (12)$$

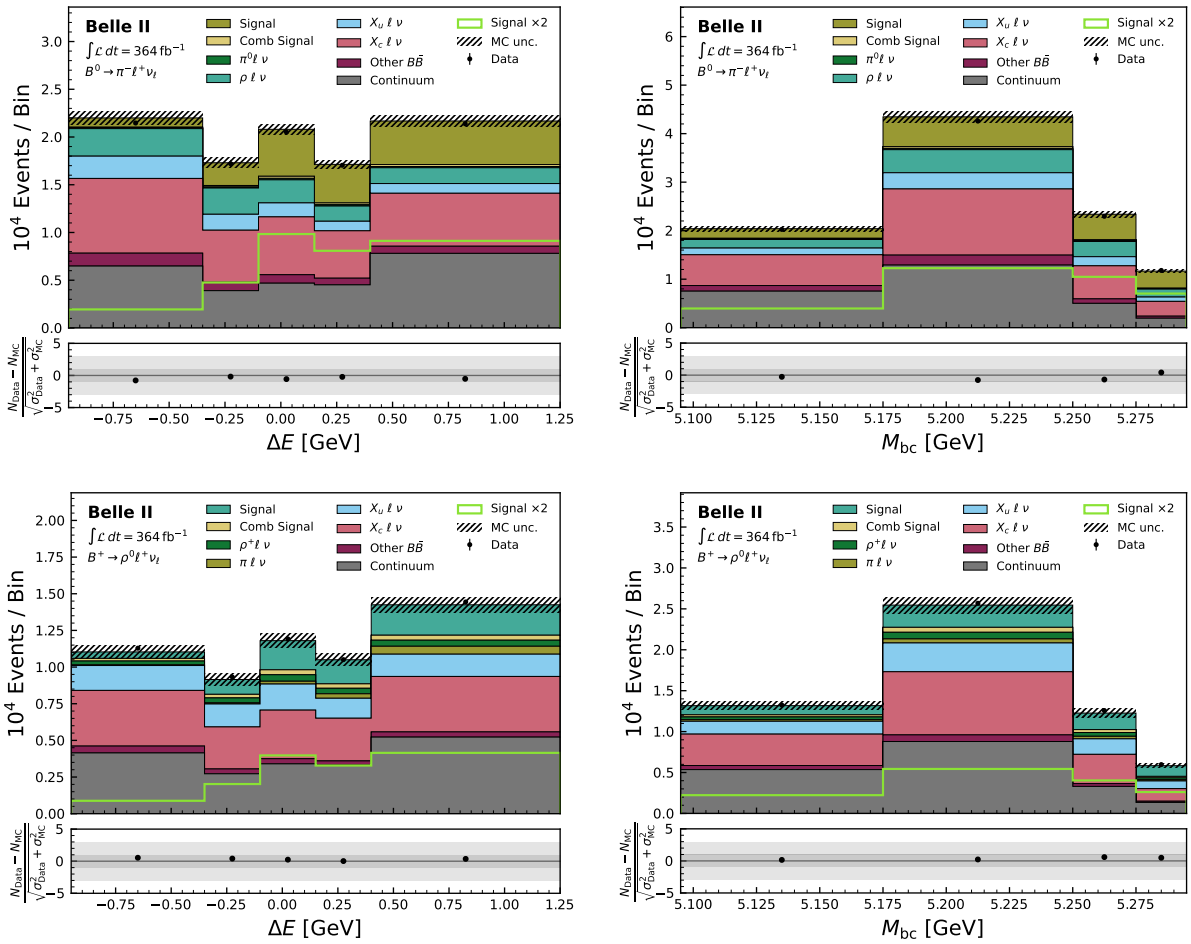

Figure 1: Distributions of ΔE (left) and M_{bc} (right) reconstructed in Belle II data integrated over the q^2 bins for $B^0 \to \pi^- \ell^+ \nu_\ell$ decays (top) and $B^+ \to \rho^0 \ell^+ \nu_\ell$ decays (bottom) with expected distributions from simulation overlaid. The simulated samples are weighted according to luminosity. The hatched areas include statistical and systematic uncertainties on the simulated distributions, discussed in Section VII. The expected signal distributions (scaled by a factor two) are also shown. The panels below the histograms show the difference between collision and simulated data divided by the combined uncertainty.

where N_l is the observed number of events in bin l, $\vec{S}$ and $\vec{B}$ are the vectors of signal and background templates, respectively, S_{lj} is the number of events in bin l of signal fit template j, and B_{lk} is the number of events in bin l of background fit template k.

B. Fit results

The fit projections of ΔE and M_{bc} in each q^2 bin are shown in Fig. 2 for the $B^0 \to \pi^- \ell^+ \nu_\ell$ and $B^+ \to \rho^0 \ell^+ \nu_\ell$ modes. The χ^2 per degree of freedom of the fit is $468.5/429 = 1.09$. The correlations between the component yields are all lower than 0.75. The highest observed correlations occur between the $B \to X_c \ell \nu_\ell$ and $B\overline{B}$ background yields in the $B^+ \to \rho^0 \ell^+ \nu_\ell$ mode. In the higher q^2 bins, the signal scale factor becomes increasingly correlated to the $B \to X_u \ell \nu_\ell$ scale factor.

Using the expected number of signal events from simulation, the fitted signal scale factors, and the signal strengths, we obtain the signal yields in each true q^2 bin, corresponding to the number of true and combinatorial signal events. The signal yields with statistical and systematic uncertainties are given in Table II. The sources of systematic uncertainty and their estimation is described in Section VII.

The partial branching fraction in true q^2 bin i is calculated using the signal yield, N_i, and the corresponding signal efficiency, ϵ_i, from

$$\Delta\mathcal{B}_i(B^0 \to \pi^- \ell^+ \nu_\ell) = \frac{N_i(1 + f_{+0})}{4\epsilon_i \times N_{B\overline{B}}}, \tag{13a}$$

$$\Delta\mathcal{B}_i(B^+ \to \rho^0 \ell^+ \nu_\ell) = \frac{N_i(1 + f_{+0})}{4\epsilon_i \times N_{B\overline{B}}} \times \frac{1}{f_{+0}}, \tag{13b}$$

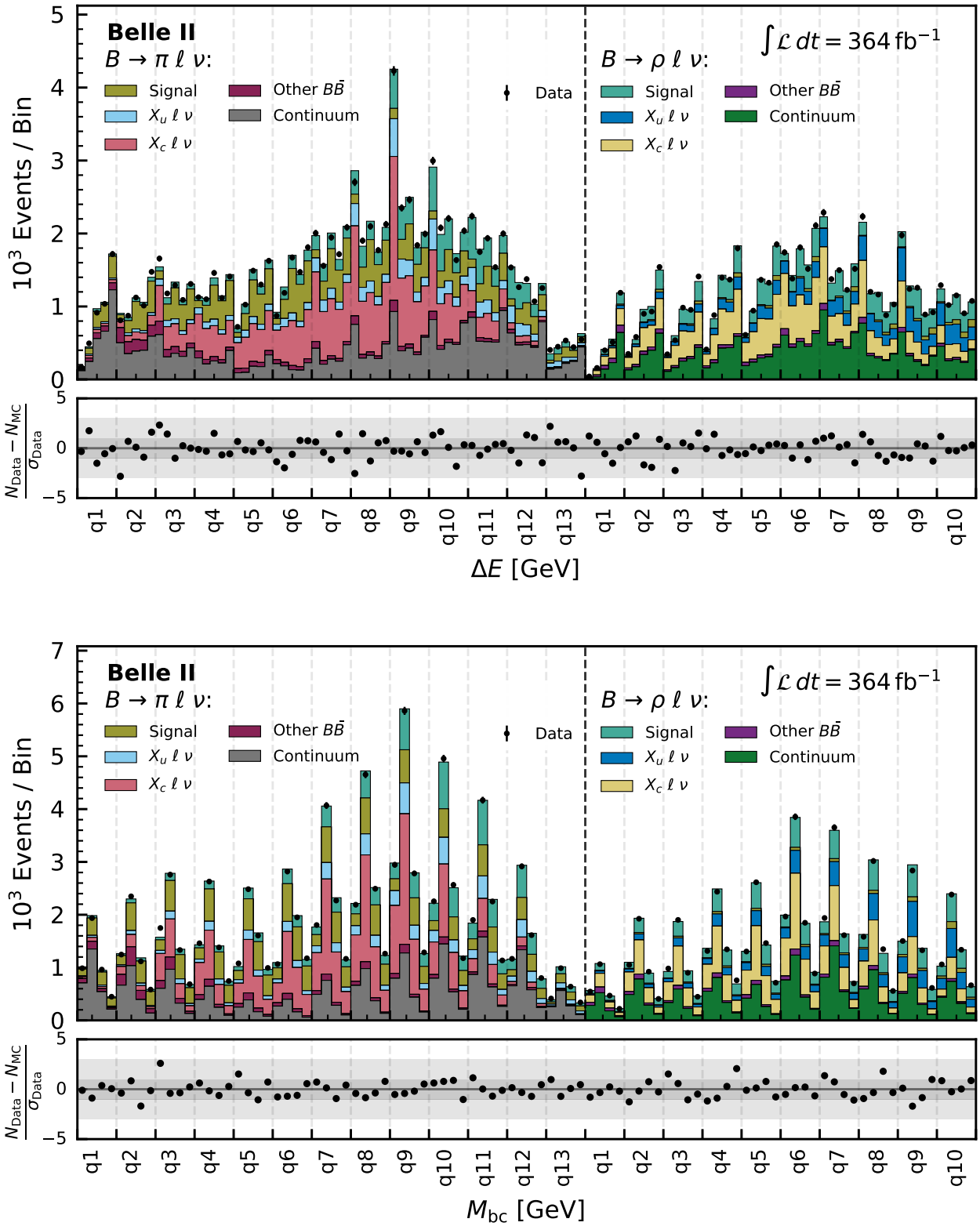

Figure 2: Distributions of ΔE (top) and M_{bc} (bottom) in the q^2 bins for $B^0 \to \pi^-\ell^+\nu_\ell$ and $B^+ \to \rho^0\ell^+\nu_\ell$ candidates reconstructed in Belle II data with fit projections overlaid. The difference between collision and simulated data divided by the data uncertainty is shown in the panels below the histograms. The boundaries of the q^2 bins are provided in the text above.

Table II: Signal yields for the $B^0 \to \pi^-\ell^+\nu_\ell$ and $B^+ \to \rho^0\ell^+\nu_\ell$ modes in each true q^2 bin with statistical and systematic uncertainties. The boundaries of the q^2 bins are given in the text above.

	Yield	
q^2 bin	$B^0 \to \pi^-\ell^+\nu_\ell$	$B^+ \to \rho^0\ell^+\nu_\ell$
$q1$	869 ± 95 ± 139	332 ± 100 ± 118
$q2$	1406 ± 123 ± 172	651 ± 114 ± 178
$q3$	1426 ± 112 ± 124	630 ± 131 ± 131
$q4$	1714 ± 120 ± 139	1028 ± 147 ± 240
$q5$	1617 ± 120 ± 113	1273 ± 158 ± 236
$q6$	2167 ± 138 ± 151	1207 ± 164 ± 244
$q7$	1817 ± 143 ± 172	962 ± 136 ± 206
$q8$	1921 ± 147 ± 181	1141 ± 118 ± 218
$q9$	1640 ± 149 ± 174	936 ± 114 ± 186
$q10$	1328 ± 142 ± 156	821 ± 96 ± 220
$q11$	1472 ± 140 ± 239	
$q12$	819 ± 120 ± 211	
$q13$	295 ± 66 ± 122	

where $f_{+0} = \mathcal{B}(\Upsilon(4S) \to B^+B^-)/\mathcal{B}(\Upsilon(4S) \to B^0\overline{B^0}) = 1.065 \pm 0.052$ [45], and $N_{B\overline{B}}$ is the number of $B\overline{B}$ pairs. The partial branching-fraction $\Delta\mathcal{B}$ results for $B^0 \to \pi^-\ell^+\nu_\ell$ and $B^+ \to \rho^0\ell^+\nu_\ell$ decays are given in Table III and shown as functions of q^2 in Fig. 3. The total correlation matrices of the partial branching fractions of $B^0 \to \pi^-\ell^+\nu_\ell$ and $B^+ \to \rho^0\ell^+\nu_\ell$ are presented in Tables IX and X in Appendix A. The central values of the partial branching fractions and the statistical and systematic covariance matrices combining both modes will be made available on HEPData [46].

Table III: Partial branching fractions $\Delta\mathcal{B}$ ($\times 10^4$) in each q^2 bin for the $B^0 \to \pi^-\ell^+\nu_\ell$ and $B^+ \to \rho^0\ell^+\nu_\ell$ modes. The first uncertainty is statistical and the second is systematic. The boundaries of the q^2 bins are provided in the text above.

	$\Delta\mathcal{B}$ ($\times 10^4$)	
q^2 bin	$B^0 \to \pi^-\ell^+\nu_\ell$	$B^+ \to \rho^0\ell^+\nu_\ell$
$q1$	0.117 ± 0.013 ± 0.019	0.109 ± 0.033 ± 0.039
$q2$	0.142 ± 0.013 ± 0.018	0.140 ± 0.025 ± 0.038
$q3$	0.119 ± 0.009 ± 0.011	0.113 ± 0.024 ± 0.024
$q4$	0.137 ± 0.010 ± 0.012	0.162 ± 0.023 ± 0.038
$q5$	0.129 ± 0.010 ± 0.010	0.193 ± 0.024 ± 0.036
$q6$	0.170 ± 0.011 ± 0.013	0.183 ± 0.025 ± 0.037
$q7$	0.139 ± 0.011 ± 0.014	0.161 ± 0.023 ± 0.035
$q8$	0.146 ± 0.011 ± 0.015	0.225 ± 0.023 ± 0.044
$q9$	0.119 ± 0.011 ± 0.013	0.182 ± 0.022 ± 0.037
$q10$	0.096 ± 0.010 ± 0.012	0.158 ± 0.019 ± 0.043
$q11$	0.109 ± 0.010 ± 0.018	
$q12$	0.065 ± 0.010 ± 0.017	
$q13$	0.028 ± 0.006 ± 0.011	

The total branching fractions determined from the sums of the partial branching fractions are

$$\mathcal{B}(B^0 \to \pi^-\ell^+\nu_\ell) = (1.516 \pm 0.042 \pm 0.059) \times 10^{-4}$$
$$\mathcal{B}(B^+ \to \rho^0\ell^+\nu_\ell) = (1.625 \pm 0.079 \pm 0.180) \times 10^{-4}$$

where the first uncertainties are statistical and the second are systematic. The results are consistent with world averages [23], and the full experimental correlation between the two values is -0.16.

We performed additional fits to test the stability of the results. We divided the data set by lepton flavor, by lepton charge, and by $\theta_{\rm miss}$ region. We then performed the fit separately for each subsample and checked that the results agree within statistical uncertainties.

VII. SYSTEMATIC UNCERTAINTIES

The fractional uncertainties on the partial branching fractions in each q^2 bin from various sources of systematic uncertainty are given in Tables IV and V. All systematic uncertainties are evaluated using the same approach. For each source of uncertainty, we vary the templates 1000 times by sampling from Gaussian distributions of the central values fully taking correlations into account. For example, to evaluate the uncertainties due to the $B \to \omega\ell\nu_\ell$ form factors, we sample 1000 alternative $B \to X_u\ell\nu_\ell$ distributions by assuming the form-factor parameter uncertainties follow Gaussian distributions. We create 1000 simplified simulated data (toy) distributions by adding the resulting variations to the remaining nominal templates. Finally, we fit the nominal templates to the toy distributions and obtain a covariance matrix of the fitted yields for each source of uncertainty using Pearson correlation [47]. Covariance matrices for the signal strengths and efficiencies are evaluated using a similar approach. The systematic uncertainties on the partial branching fractions are evaluated by propagating the covariance matrices of the fitted yields, the signal strengths and efficiencies.

A. Detector and beam-energy effects

The detector uncertainties include uncertainties arising from the tracking efficiency and the corrections to the lepton- and pion-identification efficiencies. All of these have been estimated from studies of independent data control samples.

In addition, we observe a dependence of the reconstructed q^2 resolution on the c.m. energy. Since the c.m. energy in the simulated sample differs from the mean c.m. energy in data, we account for the effect on the shape of the signal template. We investigate the effect using a control mode, in which we fully reconstruct $B^+ \to J/\psi[\to \mu^+\mu^-]K^+$ events. By ignoring one of the muons, we obtain events that are similar to signal decays with a single missing neutrino.

We determine a 4% difference in q^2 resolution between measured and simulated data in this control mode. We

Table IV: Summary of fractional uncertainties in % on the $B^0 \to \pi^- \ell^+ \nu_\ell$ partial branching fractions $\Delta\mathcal{B}$ in each q^2 bin. The boundaries of the q^2 bins are provided in the text above.

	$B^0 \to \pi^- \ell^+ \nu_\ell$												
Source	$q1$	$q2$	$q3$	$q4$	$q5$	$q6$	$q7$	$q8$	$q9$	$q10$	$q11$	$q12$	$q13$
Detector effects	2.0	0.9	1.1	1.0	1.0	1.1	1.1	1.0	0.9	1.2	2.3	4.1	5.8
Beam energy	0.6	0.8	0.7	0.8	0.7	0.6	0.6	0.6	0.5	0.5	0.5	0.6	0.7
Simulated sample size	4.7	3.8	3.3	3.2	3.2	2.9	3.8	3.7	4.0	4.5	5.9	8.0	13.6
BDT efficiency	1.3	1.3	1.3	1.3	1.3	1.3	1.3	1.3	1.3	1.3	1.3	1.3	1.3
Physics constraints	2.9	2.9	2.9	2.9	2.9	2.9	2.9	2.9	2.9	2.9	2.9	2.9	2.9
Signal model	0.1	0.1	0.2	0.1	0.0	0.2	0.2	0.4	0.3	0.8	0.9	0.2	4.9
ρ lineshape	0.1	0.1	0.3	0.3	0.2	0.1	0.3	0.1	0.3	0.1	0.2	0.2	0.6
Nonres. $B \to \pi\pi\ell\nu_\ell$	0.5	0.6	0.4	0.4	0.5	1.0	1.2	1.0	0.8	1.8	1.2	2.3	14.3
DFN parameters	0.8	0.4	1.5	1.6	1.4	1.7	1.2	0.1	0.7	1.2	2.9	3.5	3.7
$B \to X_u \ell\nu_\ell$ model	0.2	0.4	0.3	0.4	0.2	0.9	1.1	1.2	1.0	1.3	1.6	0.7	8.7
$B \to X_c \ell\nu_\ell$ model	1.4	2.0	1.7	1.3	1.3	1.4	1.8	1.6	1.3	1.4	1.1	0.5	1.7
Continuum	15.1	11.3	7.6	7.1	5.8	5.7	8.1	8.3	9.6	10.4	14.5	23.8	34.4
Total systematic	16.4	12.6	9.3	8.7	7.7	7.7	10.0	9.9	11.1	12.2	16.6	26.0	41.6
Statistical	11.0	8.8	7.9	7.0	7.5	6.4	7.9	7.7	9.1	10.7	9.6	14.6	22.6
Total	19.7	15.4	12.2	11.2	10.7	10.0	12.7	12.6	14.4	16.3	19.1	29.8	47.3

Table V: Summary of fractional uncertainties in % on the $B^+ \to \rho^0 \ell^+ \nu_\ell$ partial branching fractions $\Delta\mathcal{B}$ in each q^2 bin. The boundaries of the q^2 bins are provided in the text above.

	$B^+ \to \rho^0 \ell^+ \nu_\ell$									
Source	$q1$	$q2$	$q3$	$q4$	$q5$	$q6$	$q7$	$q8$	$q9$	$q10$
Detector effects	2.8	2.0	1.6	1.1	1.7	1.9	2.4	1.4	1.4	1.6
Beam energy	2.1	1.9	1.9	1.5	1.3	1.1	1.0	0.9	0.8	0.5
Simulated sample size	14.1	7.8	7.4	6.3	6.3	5.2	6.4	5.6	6.2	7.3
BDT efficiency	1.6	1.6	1.6	1.6	1.6	1.6	1.6	1.6	1.6	1.6
Physics constraints	2.8	2.8	2.8	2.8	2.8	2.8	2.8	2.8	2.8	2.8
Signal model	0.7	0.2	0.2	0.2	0.3	0.4	0.5	0.3	1.8	2.4
ρ lineshape	1.7	1.6	2.0	1.0	1.9	1.8	1.4	0.9	1.6	1.7
Nonres. $B \to \pi\pi\ell\nu_\ell$	5.6	6.3	6.7	8.6	9.3	10.7	10.1	7.0	7.8	11.8
DFN parameters	3.6	5.5	4.1	3.5	1.1	1.2	2.7	1.7	1.9	2.3
$B \to X_u \ell\nu_\ell$ model	1.7	3.0	3.8	5.0	5.8	6.1	6.3	1.9	7.2	12.4
$B \to X_c \ell\nu_\ell$ model	1.8	1.9	1.7	1.1	1.4	1.7	0.9	0.9	1.9	2.6
Continuum	31.5	24.3	17.0	19.6	13.2	14.8	16.0	16.6	15.2	18.7
Total systematic	35.6	27.5	21.0	23.5	18.8	20.5	21.6	19.4	20.2	27.0
Statistical	30.0	17.5	20.8	14.4	12.4	13.6	14.1	10.4	12.2	11.8
Total	46.6	32.6	29.6	27.6	22.6	24.6	25.8	22.0	23.6	29.5

scale the resolutions in each q^2 bin obtained from the simulated sample, and using the true q^2 values, in combination with Gaussian smearing according to the new resolutions, produce 1000 pseudo-reconstructed q^2 distributions. By combining these with the remaining unaffected templates we obtain 1000 varied toy distributions, which are then fit using the nominal templates.

B. Simulated sample size

The effect of having finite samples of simulated data is considered. The largest uncertainty contribution comes from the limited size of the simulated continuum sample. In addition to shape variations due to the number of events within each bin, we also account for migration effects in the true q^2 distribution, which results in signal-template migrations. To estimate this uncertainty, we sample, with replacement, true q^2 values from the total signal component 1000 times, split these into the true-q^2 templates, then fit these templates to the sum of the nominal templates.

C. BDT efficiency

We estimate an uncertainty to account for possible disagreements between the signal efficiencies in experimental and simulated data of the selection on the 48 BDT output classifiers. For each BDT output classifier selec-

tion, we use the $B^+ \to J/\psi[\to \mu^+\mu^-]K^+$ control mode discussed above to determine the ratio between the efficiency in experimental and simulated data. The ratios are in agreement with unity within uncertainties.

To account for these uncertainties we separately evaluate the standard deviations of the ratios for each type of BDT and mode and assign these as uncertainties on the signal efficiencies. We obtain uncertainties of 1.1% and 0.6% on the efficiencies of the selection on the continuum suppression BDTs in the $B^0 \to \pi^-\ell^+\nu_\ell$ and $B^+ \to \rho^0\ell^+\nu_\ell$ modes, respectively. For the $B\overline{B}$ suppression BDTs the uncertainties on the efficiencies are 0.7% and 1.5% for the $B^0 \to \pi^-\ell^+\nu_\ell$ and $B^+ \to \rho^0\ell^+\nu_\ell$ modes, respectively.

D. Physics constraints

We consider additional systematic uncertainties from the number of $B\overline{B}$ pairs $N_{B\overline{B}}$ and the branching fraction ratio of $\Upsilon(4S) \to B\overline{B}$, f_{+0}. These affect the calculation of the partial branching fractions from the yields. The uncertainty on $N_{B\overline{B}}$ results in a relative uncertainty of 1.4%, while the uncertainty on f_{+0} contributes uncertainties of 2.5% and 2.4% to the uncertainties on the partial branching fractions for $B^0 \to \pi^-\ell^+\nu_\ell$ and $B^+ \to \rho^0\ell^+\nu_\ell$, respectively.

In addition, we assign an uncertainty to the assumption of isospin-symmetry. The assumption discussed in Section V A relies on the B lifetime ratio $\tau_+/\tau_0 = 1.076 \pm 0.004$ [23]. To estimate the effect on the signal yields, we vary the relative fraction of neutral and charged B modes in the signal templates by sampling Gaussian variations of the fractions within the relative uncertainty of 0.4%.

E. Signal model and ρ lineshape

There are three ways in which the signal form-factor and branching-fraction uncertainties may impact our results. The first is the residual signal form-factor model dependence of the signal templates. Since the signal is extracted in multiple bins of true q^2, and therefore the fit is allowed to coarsely modify the q^2 spectrum, this contribution is small but not negligible. The second effect comes from signal form-factor and branching-fraction uncertainties on the composition of the background $B \to X_u\ell\nu_\ell$ template, which propagate through the fit to uncertainties on the signal yields.

The third effect accounts for bin migrations between the true q^2 bins due to signal form-factor uncertainties. These are reflected in uncertainties on the signal strengths. The assigned uncertainties are smaller than the ones originating from the dependence of the background $B \to X_u\ell\nu_\ell$ template on the signal model, but they are larger than the ones due to the residual signal-template dependence. The combination of these uncertainties is included in the signal model category in Tables IV and V.

There is an additional uncertainty source concerning the modeling of the $B^+ \to \rho^0\ell^+\nu_\ell$ signal related to the lineshape of the ρ meson. We account for a possible ρ-ω interference resulting in a change in the ρ lineshape. In Ref. [35] an amplitude fit incorporating the interference term is performed to the di-pion invariant mass spectrum measured in Ref. [29] and 1σ variations of the diagonalized fit-parameter uncertainties are obtained. We vary the lineshape of all true ρ mesons for each eigenvariation, repeat the fit, and take the largest change in fit results from the model without ρ-ω interference as the systematic uncertainty.

F. $B \to X_u\ell\nu_\ell$ background

1. *Nonresonant $B \to \pi\pi\ell\nu_\ell$ component*

One contribution to the $B \to X_u\ell\nu_\ell$ background uncertainties is related to the treatment of the nonresonant $B \to \pi\pi\ell\nu_\ell$ component, which was described in Section III C. In addition to the measured partial branching-fraction spectrum, Ref. [29] also provides the corresponding covariance matrix. We therefore vary the partial branching fractions according to this covariance matrix to determine the uncertainty on our signal yields. Overall, this results in the largest contribution to the uncertainties originating from the $B \to X_u\ell\nu_\ell$ background.

2. *DFN parameters*

A second uncertainty component comes from the uncertainty in the DFN shape function parameters that define the shape of the nonresonant $B \to X_u\ell\nu_\ell$ background. We follow the procedure of Ref. [3] to evaluate the uncertainties on the relevant parameters provided in Ref. [31]. Next, we generate simulated samples of nonresonant $B \to X_u\ell\nu_\ell$ events based on these varied parameters and reweight our nominal samples to match the varied samples. We then estimate the uncertainties by sampling 1000 toy distributions in agreement with Gaussian variations of these parameters. We also compare to a different nonresonant $B \to X_u\ell\nu_\ell$ model [48] and refrain from adding any additional uncertainties due to this, since the current uncertainties already cover any difference introduced by the change in model.

3. *$B \to X_u\ell\nu_\ell$ model*

Finally, we evaluate the uncertainties due to the $B \to \omega\ell\nu_\ell$, $B \to \eta\ell\nu_\ell$, and $B \to \eta'\ell\nu_\ell$ form factors, and obtain uncertainties shown under the $B \to X_u\ell\nu_\ell$ category. This category also includes the effects of uncertainties of

the exclusive and inclusive $B \to X_u \ell \nu_\ell$ branching fractions, except for the $B \to \pi \ell \nu_\ell$ and $B \to \rho \ell \nu_\ell$ branching fractions.

G. $B \to X_c \ell \nu_\ell$ model

The $B \to X_c \ell \nu_\ell$ model category in Tables IV and V includes the effects of the uncertainties of the $B \to D \ell \nu_\ell$ and $B \to D^* \ell \nu_\ell$ form-factor parameters, and the exclusive and inclusive $B \to X_c \ell \nu_\ell$ branching fractions. For the $B^0 \to \pi^- \ell^+ \nu_\ell$ mode this contribution to the total systematic uncertainty is larger than that of the $B \to X_u \ell \nu_\ell$ model at low q^2, but smaller at high q^2. It is subdominant over the entire q^2 range for the $B^+ \to \rho^0 \ell^+ \nu_\ell$ mode.

H. Continuum reweighting

The limited off-resonance sample size affects the continuum weights obtained during the reweighting procedure, since the weights are calculated using the number of off-resonance events within each bin. To account for the uncertainties of these numbers, we produce a set of 1000 continuum weights by recalculating the weights using bin-wise off-resonance event numbers drawn from the corresponding Poisson distributions. We then proceed with the usual procedure for determining systematic uncertainties described above. The resulting uncertainties dominate both in the $B^0 \to \pi^- \ell^+ \nu_\ell$ and $B^+ \to \rho^0 \ell^+ \nu_\ell$ mode, and are especially large in those q^2 bins where the continuum background component is largest.

VIII. $|V_{ub}|$ DETERMINATION

We extract $|V_{ub}|$ separately from $B^0 \to \pi^- \ell^+ \nu_\ell$ and $B^+ \to \rho^0 \ell^+ \nu_\ell$ using χ^2 fits to the measured q^2 spectra. The χ^2 is defined as

$$\chi^2 = \sum_{i,j=1}^{N} (\Delta\mathcal{B}_i - \Delta\Gamma_i \tau) C_{ij}^{-1} (\Delta\mathcal{B}_j - \Delta\Gamma_j \tau) + \sum_m \chi^2_{\text{Theory},m}, \quad (14)$$

where C_{ij}^{-1} is the inverse total covariance matrix of the measured partial branching fractions $\Delta\mathcal{B}_i$ in bin i, and N is the number of q^2 bins. The quantities $\Delta\Gamma_i$ contain the predictions for the differential decay rates in bin i, τ is the B lifetime, and $\chi^2_{\text{Theory},m}$ incorporates the constraints from theory calculation m. The predictions for the differential decay rates provided in Equations 2 and 3 include the form factors and $|V_{ub}|$.

For $B^0 \to \pi^- \ell^+ \nu_\ell$ we include LQCD constraints on three $f_+(q^2)$ BCL form-factor coefficients b_k^+ and two $f_0(q^2)$ BCL form-factor coefficients b_k^0 given in Equations 5 and 6, respectively, as nuisance parameters. The nuisance parameters constrain the shape and normalization of the relevant form factors entering the differential decay rate and allow for a determination of $|V_{ub}|$. In the evaluation of the inverse Blaschke factors for the expansion of $f_+(q^2)$ in Equation 5, m_R takes the value of 5.325 GeV [8]. The χ^2_{LQCD} term takes the form:

$$\chi^2_{\text{LQCD}} = \sum_{k,l=1}^{5} (b_k - b_k^{\text{LQCD}}) C^{-1}_{\text{LQCD},kl} (b_l - b_l^{\text{LQCD}}), \quad (15)$$

where the constraints on the form-factor coefficients b_k^{LQCD} and the corresponding inverse covariance matrix $C^{-1}_{\text{LQCD},kl}$ are taken from the latest version of the FLAG 21 review (February 2023) [4], and combine results from the FNAL/MILC [49], RBC/UKQCD [50], and JLQCD [51] collaborations.

In addition to the LQCD constraints, we may also add LCSR constraints from Ref. [5], which determine $f_+(q^2)$ and $f_0(q^2)$ at five points in q^2. In this case the additional χ^2_{LCSR} term takes the form:

$$\chi^2_{\text{LCSR}} = \sum_{k,l=1}^{10} (f_k - f_k^{\text{LCSR}}) C^{-1}_{\text{LCSR},kl} (f_l - f_l^{\text{LCSR}}). \quad (16)$$

Here we implement direct constraints on the form factors f_k ($f_+(q^2)$ and $f_0(q^2)$) from LCSR predictions f_k^{LCSR}, taking the corresponding inverse covariance matrix $C^{-1}_{\text{LCSR},kl}$ into account.

The result for $|V_{ub}|$ from the $B^0 \to \pi^- \ell^+ \nu_\ell$ mode using only the LQCD constraints is:

$$|V_{ub}|_{B \to \pi \ell \nu_\ell} = (3.93 \pm 0.09 \pm 0.13 \pm 0.19) \times 10^{-3},$$

where for all quoted $|V_{ub}|$ results the first uncertainty is statistical, the second is systematic and the third is theoretical. Upon adding the LCSR constraints, the result for $|V_{ub}|$ from $B^0 \to \pi^- \ell^+ \nu_\ell$ becomes:

$$|V_{ub}|_{B \to \pi \ell \nu_\ell} = (3.73 \pm 0.07 \pm 0.07 \pm 0.16) \times 10^{-3}.$$

The measured central values of $|V_{ub}|$ and the BCL form-factor coefficients from the fits to the $B^0 \to \pi^- \ell^+ \nu_\ell$ spectrum are provided in Table VI. The full correlation matrices corresponding to these values are provided in Tables XI and XII in Appendix A.

For $B^+ \to \rho^0 \ell^+ \nu_\ell$ we include LCSR constraints on six BSZ coefficients b_k^i given in Equation 7 from Ref. [6]. These correspond to constraints on two coefficients each for $A_1(q^2)$, $A_2(q^2)$, and $V(q^2)$. The χ^2_{LCSR} term for the fit to the measured $B^+ \to \rho^0 \ell^+ \nu_\ell$ q^2 spectrum takes the form:

$$\chi^2_{\text{LCSR}} = \sum_{k,l=1}^{6} (b_k - b_k^{\text{LCSR}}) C^{-1}_{\text{LCSR},kl} (b_l - b_l^{\text{LCSR}}), \quad (17)$$

where b_k^{LCSR} are the constraints on the coefficients and $C^{-1}_{\text{LCSR},kl}$ is the corresponding inverse covariance matrix predicted by LCSR calculations. In the evaluation of the

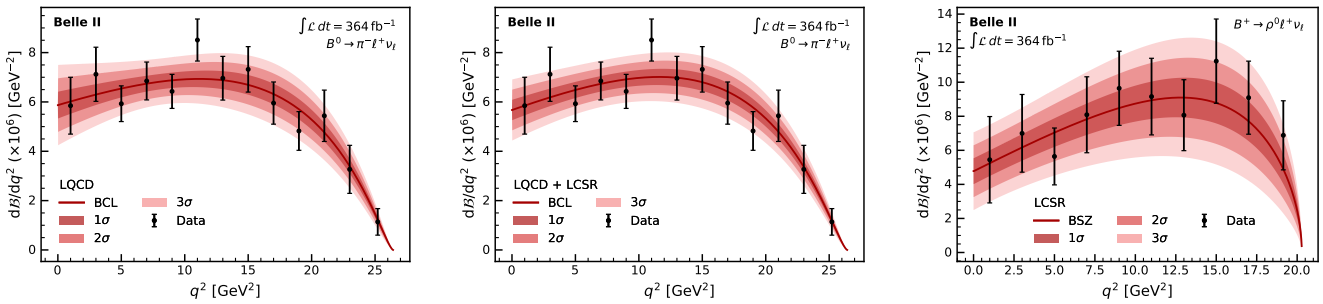

(a) (b) (c)

Figure 3: Measured partial branching fractions as a function of q^2 for $B^0 \to \pi^- \ell^+ \nu_\ell$ (a+b) and $B^+ \to \rho^0 \ell^+ \nu_\ell$ (c). The fitted differential rates are shown together with the one, two, and three standard-deviation uncertainty bands for fits using constraints on the form factors from (a) LQCD, (b) LQCD and LCSR, and (c) LCSR predictions.

Table VI: Measured central values of $|V_{ub}|$ and the BCL form-factor coefficients with total uncertainties from the fits to the $B^0 \to \pi^- \ell^+ \nu_\ell$ spectrum.

$B^0 \to \pi^- \ell^+ \nu_\ell$			
		LQCD	LQCD + LCSR
$|V_{ub}|$ (10^{-3})		3.93 ± 0.25	3.73 ± 0.19
$f_+(q^2)$	b_0^+	0.42 ± 0.02	0.45 ± 0.02
	b_1^+	-0.52 ± 0.05	-0.52 ± 0.05
	b_2^+	-0.81 ± 0.21	-1.02 ± 0.18
$f_0(q^2)$	b_0^0	0.02 ± 0.25	0.59 ± 0.02
	b_1^0	-1.43 ± 0.08	-1.39 ± 0.07
χ^2/ndf		8.39/7	8.36/7

Table VII: Measured central values of $|V_{ub}|$ and the BSZ form-factor coefficients with total uncertainties from the fit to the $B^+ \to \rho^0 \ell^+ \nu_\ell$ spectrum.

$B^+ \to \rho^0 \ell^+ \nu_\ell$		
		LCSR
$|V_{ub}|$ (10^{-3})		3.19 ± 0.33
$A_1(q^2)$	$b_0^{A_1}$	0.27 ± 0.03
	$b_1^{A_1}$	0.34 ± 0.13
$A_2(q^2)$	$b_0^{A_2}$	0.29 ± 0.03
	$b_1^{A_2}$	0.66 ± 0.17
$V(q^2)$	b_0^V	0.33 ± 0.03
	b_1^V	-0.93 ± 0.17
χ^2/ndf		3.85/3

inverse Blaschke factors for the expansion of $A_1(q^2)$ and $A_2(q^2)$ in Equation 7, m_R takes the value of 5.724 GeV, while it takes the value of 5.325 GeV for the expansion of $V(q^2)$ [6]. The $|V_{ub}|$ result obtained from $B^+ \to \rho^0 \ell^+ \nu_\ell$ using LCSR constraints is:

$$|V_{ub}|_{B \to \rho \ell \nu_\ell} = (3.19 \pm 0.12 \pm 0.17 \pm 0.26) \times 10^{-3}.$$

The measured central values of $|V_{ub}|$ and the BSZ form-factor coefficients from the fit to the $B^+ \to \rho^0 \ell^+ \nu_\ell$ spectrum are provided in Table VII. The full correlation matrix corresponding to these values is provided in Table XIII in Appendix A. Fig. 3 shows the measured and fitted differential rates of $B^0 \to \pi^- \ell^+ \nu_\ell$ and $B^+ \to \rho^0 \ell^+ \nu_\ell$, as well as the one, two, and three standard-deviation uncertainty bands from the fits.

The $|V_{ub}|$ results obtained from $B^0 \to \pi^- \ell^+ \nu_\ell$ are consistent with previous exclusive measurements [3]. The result obtained from $B^+ \to \rho^0 \ell^+ \nu_\ell$ is lower, but consistent with previous $|V_{ub}|$ determinations from $B \to \rho \ell \nu_\ell$ decays [34]. The χ^2 per degree of freedom for the fits range from 1.19 to 1.28, and are provided in Tables VI and VII for $B^0 \to \pi^- \ell^+ \nu_\ell$ and $B^+ \to \rho^0 \ell^+ \nu_\ell$, respectively. The extracted central values of $|V_{ub}|$ and the coefficients, with the corresponding full covariance matrices, for the fits to the $B^0 \to \pi^- \ell^+ \nu_\ell$ and $B^+ \to \rho^0 \ell^+ \nu_\ell$ spectra will be provided on HEPData [46]. We confirm the stability of the $|V_{ub}|$ results by repeating the fits using different q^2 cut-off values. The results are presented in Fig. 4 in Appendix B.

The fractional uncertainties on the $|V_{ub}|$ results from various sources of systematic uncertainty are shown in Table VIII. For both $B^0 \to \pi^- \ell^+ \nu_\ell$ and $B^+ \to \rho^0 \ell^+ \nu_\ell$ the largest contribution to the systematic uncertainty comes from the limited off-resonance data sample. In addition, for $B^+ \to \rho^0 \ell^+ \nu_\ell$ the systematic uncertainty from nonresonant $B \to \pi\pi\ell\nu_\ell$ is significant.

IX. SUMMARY

We extract partial branching fractions of $B^0 \to \pi^- \ell^+ \nu_\ell$ and $B^+ \to \rho^0 \ell^+ \nu_\ell$ decays reconstructed in an electron-positron collision data sample corresponding to 364 fb^{-1} collected by the Belle II experiment. The branching-fraction of $B^0 \to \pi^- \ell^+ \nu_\ell$ is found to be $(1.516 \pm 0.042(\mathrm{stat}) \pm 0.059(\mathrm{syst})) \times 10^{-4}$, and the branching fraction of $B^+ \to \rho^0 \ell^+ \nu_\ell$ is found to be

Table VIII: Summary of fractional uncertainties in % on the extracted $|V_{ub}|$ values.

	$B^0 \to \pi^-\ell^+\nu_\ell$		$B^+ \to \rho^0\ell^+\nu_\ell$
	LQCD	LQCD + LCSR	LCSR
Detector effects	0.64	0.24	0.44
Beam energy	0.05	0.03	0.09
Simulated sample size	1.51	0.78	1.41
BDT efficiency	0.31	0.21	0.28
Physics constraints	0.61	0.43	0.88
Signal model	0.38	0.13	0.41
ρ lineshape	0.26	0.21	0.13
Nonres. $B \to \pi\pi\ell\nu_\ell$	0.43	0.11	1.97
DFN parameters	0.64	0.32	0.88
$B \to X_u\ell\nu_\ell$ model	0.61	0.40	1.56
$B \to X_c\ell\nu_\ell$ model	0.51	0.43	0.50
Continuum	2.39	1.37	4.91
Total systematic	3.26	1.91	5.33
Statistical	2.31	1.82	3.76
Theory	4.83	4.29	8.15
Total	6.40	5.13	10.34

$(1.625 \pm 0.079(\text{stat}) \pm 0.180(\text{syst})) \times 10^{-4}$. These are consistent with the current world averages [23].

We extract values of the CKM matrix-element magnitude $|V_{ub}|$ from $B^0 \to \pi^-\ell^+\nu_\ell$ decays using LQCD constraints provided by the FLAG 21 review (updated February 2023) [4]. We obtain $(3.93 \pm 0.09(\text{stat}) \pm 0.13(\text{syst}) \pm 0.19(\text{theo})) \times 10^{-3}$. Using additional constraints from LCSR [5] this result becomes $(3.73 \pm 0.07(\text{stat}) \pm 0.07(\text{syst}) \pm 0.16(\text{theo})) \times 10^{-3}$. The $|V_{ub}|$ result obtained from the measurement of $B^+ \to \rho^0\ell^+\nu_\ell$ with constraints from LCSR [6] is $(3.19 \pm 0.12(\text{stat}) \pm 0.18(\text{syst}) \pm 0.26(\text{theo})) \times 10^{-3}$.

Currently our results are limited by the size of the off-resonance data set and the description of the nonresonant $B \to X_u\ell\nu_\ell$ background. The first uncertainty could be reduced by improvements in the simulation of continuum backgrounds.

This work, based on data collected using the Belle II detector, which was built and commissioned prior to March 2019, was supported by Higher Education and Science Committee of the Republic of Armenia Grant No. 23LCG-1C011; Australian Research Council and Research Grants No. DP200101792, No. DP210101900, No. DP210102831, No. DE220100462, No. LE210100098, and No. LE230100085; Austrian Federal Ministry of Education, Science and Research, Austrian Science Fund No. P 31361-N36 and No. J4625-N, and Horizon 2020 ERC Starting Grant No. 947006 "InterLeptons"; Natural Sciences and Engineering Research Council of Canada, Compute Canada and CANARIE; National Key R&D Program of China under Contract No. 2022YFA1601903, National Natural Science Foundation of China and Research Grants No. 11575017, No. 11761141009, No. 11705209, No. 11975076, No. 12135005, No. 12150004, No. 12161141008, and No. 12175041, and Shandong Provincial Natural Science Foundation Project ZR2022JQ02; the Czech Science Foundation Grant No. 22-18469S; European Research Council, Seventh Framework PIEF-GA-2013-622527, Horizon 2020 ERC-Advanced Grants No. 267104 and No. 884719, Horizon 2020 ERC-Consolidator Grant No. 819127, Horizon 2020 Marie Sklodowska-Curie Grant Agreement No. 700525 "NIOBE" and No. 101026516, and Horizon 2020 Marie Sklodowska-Curie RISE project JENNIFER2 Grant Agreement No. 822070 (European grants); L'Institut National de Physique Nucléaire et de Physique des Particules (IN2P3) du CNRS and L'Agence Nationale de la Recherche (ANR) under grant ANR-21-CE31-0009 (France); BMBF, DFG, HGF, MPG, and AvH Foundation (Germany); Department of Atomic Energy under Project Identification No. RTI 4002, Department of Science and Technology, and UPES SEED funding programs No. UPES/R&D-SEED-INFRA/17052023/01 and No. UPES/R&D-SOE/20062022/06 (India); Israel Science Foundation Grant No. 2476/17, U.S.-Israel Binational Science Foundation Grant No. 2016113, and Israel Ministry of Science Grant No. 3-16543; Istituto Nazionale di Fisica Nucleare and the Research Grants BELLE2; Japan Society for the Promotion of Science, Grant-in-Aid for Scientific Research Grants No. 16H03968, No. 16H03993, No. 16H06492, No. 16K05323, No. 17H01133, No. 17H05405, No. 18K03621, No. 18H03710, No. 18H05226, No. 19H00682, No. 20H05850, No. 20H05858, No. 22H00144, No. 22K14056, No. 22K21347, No. 23H05433, No. 26220706, and No. 26400255, the National Institute of Informatics, and Science Information NETwork 5 (SINET5), and the Ministry of Education, Culture, Sports, Science, and Technology (MEXT) of Japan; National Research Foundation (NRF) of Korea Grants No. 2016R1D1A1B02012900, No. 2018R1A2B3003643, No. 2018R1A6A1A06024970, No. 2019R1I1A3A01058933, No. 2021R1A6A1A-03043957, No. 2021R1F1A1060423, No. 2021R1F1A-1064008, No. 2022R1A2C1003993, and No. RS-2022-00197659, Radiation Science Research Institute, Foreign Large-Size Research Facility Application Supporting project, the Global Science Experimental Data Hub Center of the Korea Institute of Science and Technology Information and KREONET/GLORIAD; Universiti Malaya RU grant, Akademi Sains Malaysia, and Ministry of Education Malaysia; Frontiers of Science Program Contracts No. FOINS-296, No. CB-221329, No. CB-236394, No. CB-254409, and No. CB-180023, and SEP-CINVESTAV Research Grant No. 237 (Mexico); the Polish Ministry of Science and Higher Education and the National Science Center; the Ministry of Science and Higher Education of the Russian Federation and the HSE University Basic Research Program, Moscow; University of Tabuk Research Grants No. S-0256-1438 and No. S-0280-1439 (Saudi Arabia); Slovenian Research

Agency and Research Grants No. J1-9124 and No. P1-0135; Agencia Estatal de Investigacion, Spain Grant No. RYC2020-029875-I and Generalitat Valenciana, Spain Grant No. CIDEGENT/2018/020; National Science and Technology Council, and Ministry of Education (Taiwan); Thailand Center of Excellence in Physics; TUBITAK ULAKBIM (Turkey); National Research Foundation of Ukraine, Project No. 2020.02/0257, and Ministry of Education and Science of Ukraine; the U.S. National Science Foundation and Research Grants No. PHY-1913789 and No. PHY-2111604, and the U.S. Department of Energy and Research Awards No. DE-AC06-76RLO1830, No. DE-SC0007983, No. DE-SC0009824, No. DE-SC0009973, No. DE-SC0010007, No. DE-SC0010073, No. DE-SC0010118, No. DE-SC0010504, No. DE-SC0011784, No. DE-SC0012704, No. DE-SC0019230, No. DE-SC0021274, No. DE-SC0021616, No. DE-SC0022350, No. DE-SC0023470; and the Vietnam Academy of Science and Technology (VAST) under Grants No. NVCC.05.12/22-23 and No. DL0000.02/24-25.

These acknowledgements are not to be interpreted as an endorsement of any statement made by any of our institutes, funding agencies, governments, or their representatives.

We thank the SuperKEKB team for delivering high-luminosity collisions; the KEK cryogenics group for the efficient operation of the detector solenoid magnet; the KEK computer group and the NII for on-site computing support and SINET6 network support; and the raw-data centers at BNL, DESY, GridKa, IN2P3, INFN, and the University of Victoria for off-site computing support.

[1] M. Kobayashi and T. Maskawa. Prog. Theor. Phys. **49** (1973) 652.
[2] N. Cabibbo. Phys. Rev. Lett. **10** (1963) 531.
[3] Y. S. Amhis et al. (Heavy Flavor Averaging Group), Phys. Rev. D **107** (2023) .
[4] Y. Aoki et al. (Flavour Lattice Averaging Group), Eur. Phys. J. C **82** (2023) 869.
[5] D. Leljak, B. Melic and D. van Dyk. J. High Energ. Phys. **36** (2021) .
[6] A. Bharucha, D. M. Straub and R. Zwicky. J. High Energ. Phys. **98** (2016) .
[7] J. Dingfelder and T. Mannel. Rev. Mod. Phys. **88** (2016) 035008.
[8] C. Bourrely, L. Lellouch and I. Caprini. Phys. Rev. D **79** (2009) .
[9] T. Abe et al. (Belle II Collaboration), `arXiv:1011.0352`.
[10] K. Akai, K. Furukawa and H. Koiso. (SuperKEKB Collaboration), Nucl. Instrum. Meth. A **907** (2018) 188.
[11] K. Adamczyk et al. (Belle II SVD Collaboration), JINST **17** (2022) P11042.
[12] D. Kotchetkov et al. Nucl. Instrum. Meth. A **941** (2019) 162342.
[13] D. J. Lange. Nucl. Instrum. Meth. A **462** (2001) 152.
[14] T. Sjöstrand et al. Comput. Phys. Commun. **191** (2015) 159.
[15] S. Jadach, B. F. L. Ward and Z. Wąs. Comput. Phys. Commun. **130** (2000) 260.
[16] S. Jadach, J. H. Kuhn and Z. Wąs. Comput. Phys. Commun. **64** (1990) 275.
[17] F. A. Berends and R. van Gulik. Comput. Phys. Commun. **144** (2002) 82.
[18] E. Barberio, B. van Eijk and Z. Wąs. Comput. Phys. Commun. **66** (1991) 115.
[19] A. Natochii et al. `arXiv:2203.05731`.
[20] S. Agostinelli et al. (GEANT4 Collaboration), Nucl. Instrum. Meth. A **506** (2003) 250.
[21] T. Kuhr, C. Pulvermacher, M. Ritter, T. Hauth and N. Braun. Comput. Softw. Big Sci. **3** (2019) 1.
[22] Belle II Collaboration. *Belle II Analysis Software Framework (basf2)*, 2022. 10.5281/zenodo.5574115.
[23] P. A. Zyla et al. (Particle Data Group), PTEP **2020 8** (2020) 083C01.
[24] F. U. Bernlochner and Z. Ligeti. Phys. Rev. D **95** (2017) .
[25] F. Abudinén et al. (Belle II Collaboration), Phys. Rev. D **107** (2023) 072002.
[26] C. G. Boyd, B. Grinstein and R. F. Lebed. Phys. Rev. Lett. **74** (1995) 4603.
[27] R. Glattauer et al. (Belle Collaboration), Phys. Rev. D **93** (2016) .
[28] D. Ferlewicz, P. Urquijo and E. Waheed. Phys. Rev. D **103** (2021) .
[29] C. Beleño et al. (Belle Collaboration), Phys. Rev. D **103** (2021) .
[30] F. De Fazio and M. Neubert. J. High Energ. **06** (1999) 017.
[31] O. L. Buchmüller and H. U. Flächer. Phys. Rev. D **73** (2006) 073008.
[32] C. Ramirez, J. F. Donoghue and G. Burdman. Phys. Rev. D **41** (1990) 1496.
[33] M. T. Prim et al. (Belle Collaboration), Phys. Rev. D **101** (2020) .
[34] F. U. Bernlochner, M. T. Prim and D. J. Robinson. Phys. Rev. D **104** (2021) .
[35] F. U. Bernlochner and S. Wallner. Phys. Rev. D **109** (2024) 074040.
[36] G. Duplancic and B. Melic. J. High Energ. **11** (2015) 138.
[37] J. F. Krohn, F. Tenchini, P. Urquijo et al. Nucl. Instrum. Meth. A **976** (2020) 164269.
[38] B. Aubert et al. (BABAR Collaboration), Phys. Rev. D **74** (2006) .
[39] E. Waheed et al. (Belle Collaboration), Phys. Rev. D **100** (2019) .
[40] I. Adachi et al. (Belle II Collaboration), Phys. Rev. D **108** (2023) 092013.
[41] T. Keck. Comput. Softw. Big Sci. **1** (2016) 2.
[42] G. C. Fox and S. Wolfram. Phys. Rev. Lett. **41** (1978) 1581.
[43] A. J. Bevan, B. Golob, T. Mannel, S. Prell, B. D. Yabsley et al. Eur. Phys. J. C **74** (2014) 3026.
[44] D. M. Asner et al. (CLEO Collaboration), Phys. Rev. D **53** (1996) 1039.

[45] S. Choudhury et al. (Belle Collaboration), Phys. Rev. D **107** (2023) L031102.
[46] `HEPDATA,NEEDTOMAKETHIS`.
[47] J. Benesty, J. Chen, Y. Huang and I. Cohen. *Noise Reduction in Speech Processing* (Springer, Berlin, Heidelberg, 2009), vol. 2, pp. 1–4.
[48] M. N. Björn O. Lange and G. Paz. Phys. Rev. D **72** (2005) .
[49] J. A. Bailey et al. (Fermilab Lattice and MILC Collaborations), Phys. Rev. D **92** (2015) .
[50] J. M. Flynn et al. (RBC and UKQCD Collaborations), Phys. Rev. D **91** (2015) 074510.
[51] B. Colquhoun et al. (JLQCD Collaboration), Phys. Rev. D **106** (2022) 054502.

Appendix A: Correlation matrices

Tables IX and X show the full experimental covariance matrices for the measurements of the $B^0 \to \pi^- \ell^+ \nu_\ell$ and $B^+ \to \rho^0 \ell^+ \nu_\ell$ partial branching fractions $\Delta\mathcal{B}$, respectively. In addition, Tables XI and XII contain the full correlation matrices of the measurements of $|V_{ub}|$ and the form-factor coefficients from $B^0 \to \pi^- \ell^+ \nu_\ell$ using constraints from LQCD or from LQCD in combination with LCSR. Table XIII presents the full correlation matrix of the $|V_{ub}|$ and form-factor coefficient measurement from $B^+ \to \rho^0 \ell^+ \nu_\ell$ using LCSR constraints.

Appendix B: $|V_{ub}|$ stability test

Fig. 4 presents the values of $|V_{ub}|$ extracted when different q^2 cut-off values are used during the χ^2 fits.

Table IX: Total correlation matrix of the partial branching fractions $\Delta\mathcal{B}$ for $B^0 \to \pi^-\ell^+\nu_\ell$.

q^2 bin	$q1$	$q2$	$q3$	$q4$	$q5$	$q6$	$q7$	$q8$	$q9$	$q10$	$q11$	$q12$	$q13$
$q1$	1.000												
$q2$	0.021	1.000											
$q3$	0.105	−0.193	1.000										
$q4$	−0.018	0.019	−0.139	1.000									
$q5$	−0.031	−0.052	0.202	−0.053	1.000								
$q6$	0.065	−0.058	0.034	0.097	0.004	1.000							
$q7$	−0.097	−0.160	0.069	0.226	0.223	0.090	1.000						
$q8$	−0.067	−0.097	0.026	0.026	0.194	0.255	0.213	1.000					
$q9$	0.088	0.035	−0.019	−0.027	0.053	0.170	0.108	0.110	1.000				
$q10$	0.007	−0.007	0.001	−0.053	0.067	0.100	0.050	0.058	0.196	1.000			
$q11$	0.075	0.001	0.059	−0.005	0.021	0.056	0.028	−0.035	0.148	0.236	1.000		
$q12$	0.050	0.080	0.014	0.004	−0.035	−0.044	−0.038	−0.101	0.074	0.187	0.297	1.000	
$q13$	0.030	−0.053	0.115	0.024	0.041	−0.048	−0.011	−0.078	−0.092	−0.129	−0.212	−0.355	1.000

Table X: Total correlation matrix of the partial branching fractions $\Delta\mathcal{B}$ for $B^+ \to \rho^0\ell^+\nu_\ell$.

q^2 bin	$q1$	$q2$	$q3$	$q4$	$q5$	$q6$	$q7$	$q8$	$q9$	$q10$
$q1$	1.000									
$q2$	−0.340	1.000								
$q3$	0.146	−0.322	1.000							
$q4$	0.023	0.241	−0.241	1.000						
$q5$	−0.052	0.131	0.275	−0.060	1.000					
$q6$	0.017	0.139	0.183	0.464	0.148	1.000				
$q7$	−0.021	0.197	0.068	0.184	0.428	0.030	1.000			
$q8$	0.149	0.018	0.054	0.216	0.205	0.311	−0.063	1.000		
$q9$	0.095	0.101	0.050	0.115	0.136	0.156	0.235	−0.005	1.000	
$q10$	0.004	0.187	−0.083	0.153	0.151	0.133	0.188	0.341	0.241	1.000

Table XI: Full correlation matrix of $|V_{ub}|$ and the BCL form-factor coefficients from the fit to the $B^0 \to \pi^-\ell^+\nu_\ell$ spectrum with LQCD constraints.

	$\lvert V_{ub}\rvert$	b_0^+	b_1^+	b_2^+	b_0^0	b_1^0
$\lvert V_{ub}\rvert$	1.000					
b_0^+	−0.806	1.000				
b_1^+	−0.053	−0.273	1.000			
b_2^+	0.062	−0.319	−0.338	1.000		
b_0^0	−0.315	0.409	−0.073	−0.204	1.000	
b_1^0	−0.142	−0.048	0.150	0.258	−0.775	1.000

Table XII: Full correlation matrix of $|V_{ub}|$ and the BCL form-factor coefficients from the fit to the $B^0 \to \pi^-\ell^+\nu_\ell$ spectrum with LQCD and LCSR constraints.

	$\lvert V_{ub}\rvert$	b_0^+	b_1^+	b_2^+	b_0^0	b_1^0
$\lvert V_{ub}\rvert$	1.000					
b_0^+	−0.791	1.000				
b_1^+	0.007	−0.339	1.000			
b_2^+	0.243	−0.375	−0.448	1.000		
b_0^0	−0.376	0.430	−0.065	−0.190	1.000	
b_1^0	0.003	−0.164	0.127	0.244	−0.830	1.000

Table XIII: Full correlation matrix of $|V_{ub}|$ and the BSZ form-factor coefficients from the fit to the $B^+ \to \rho^0 \ell^+ \nu_\ell$ spectrum with LCSR constraints.

	$\lvert V_{ub}\rvert$	$b_0^{A_1}$	$b_1^{A_1}$	$b_0^{A_2}$	$b_1^{A_2}$	b_0^{V}	b_1^{V}
$\lvert V_{ub}\rvert$	1.000						
$b_0^{A_1}$	−0.464	1.000					
$b_1^{A_1}$	0.035	0.542	1.000				
$b_0^{A_2}$	−0.735	0.241	−0.117	1.000			
$b_1^{A_2}$	−0.126	−0.007	0.023	0.472	1.000		
b_0^{V}	−0.473	0.894	0.493	0.255	−0.056	1.000	
b_1^{V}	0.064	0.538	0.946	−0.144	0.127	0.558	1.000

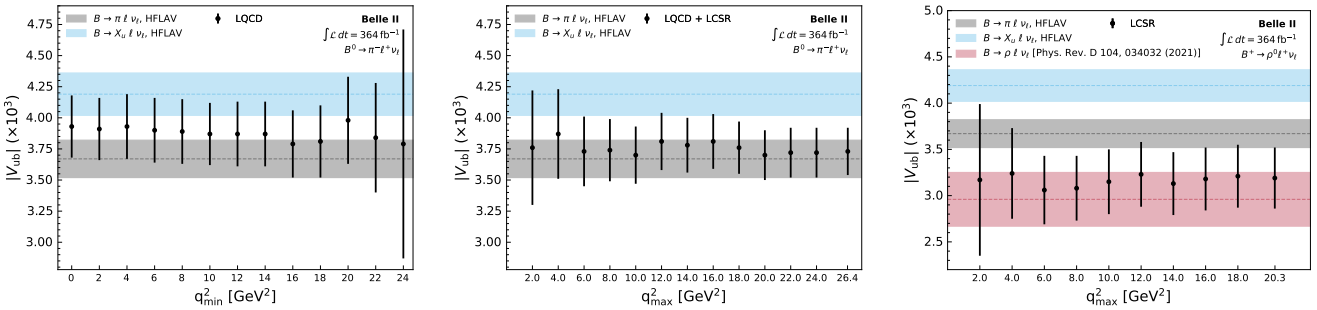

(a) (b) (c)

Figure 4: Measured $|V_{ub}|$ values from $B^0 \to \pi^- \ell^+ \nu_\ell$ (a+b) and $B^+ \to \rho^0 \ell^+ \nu_\ell$ (c) for different cut-off values of q^2 in the fit. In (a), where only LQCD constraints are used, minimum cut-off values are tested, while in (b+c), where LCSR constraints are used, maximum cut-off values are tested. We also show a comparison to the world-average $|V_{ub}|$ values from $B \to \pi \ell \nu_\ell$ and inclusive $B \to X_u \ell \nu_\ell$ from Ref. [3]. In (c) we further compare to the $|V_{ub}|$ result obtained in Ref. [34] from $B \to \rho \ell \nu_\ell$ measurements.